Commun Nonlinear Sci Numer Simulat 102 (2021) 105948

Contents lists available at ScienceDirect

Commun Nonlinear Sci Numer Simulat

journal homepage: www.elsevier.com/locate/cnsns

Research paper

Using invariant manifolds to capture an asteroid near the L_3 point of the Earth-Moon Bicircular model

Àngel Jorba, Begoña Nicolás*

Departament de Matemàtiques i Informàtica, Barcelona Graduate School of Mathematics (BGSMath), Universitat de Barcelona (UB), Gran Via de les Corts Catalanes 585, Barcelona 08007, Spain

ARTICLE INFO

Article history:
Available online 3 July 2021

Keywords:
Parametrization method
Quasi-periodic orbits
Asteroid capture
Jet transport

ABSTRACT

This paper focuses on the capture of Near-Earth Asteroids (NEAs) in a neighbourhood of the L_3 point of the Earth-Moon system. The dynamical model for the motion of the asteroid is the planar Earth-Moon-Sun Bicircular problem (BCP). It is known that the L_3 point of the Restricted Three-Body Problem is replaced, in the BCP, by a periodic orbit of centre×saddle type, with a family of mildly hyperbolic tori that is born from the elliptic direction of this periodic orbit. It is remarkable that some pieces of the stable manifolds of these tori escape (backward in time) the Earth-Moon system and become nearly circular orbits around the Sun. In this work we compute this family of invariant tori and also high order approximations to their stable/unstable manifolds. We show how to use these manifolds to compute an impulsive transfer of a NEA to an invariant tori near L_3. As an example, we study the capture of the asteroid 2006 RH120 in its approach of 2006. We show that there are several opportunities for this capture, with different costs. It is remarkable that one of them requires a Δv as low as 20 m/s.

1. Introduction

Today, several space agencies and private companies are considering the exploitation of raw materials from asteroids, e.g., gold, iridium and platinum [1,29,37]. Metals such as gold or platinum could be transported to Earth, while more common metals could be used for construction in space [30]. Different options have been pointed out to obtain these materials from asteroids. One option is to send a robotic probe to visit an asteroid, collect such materials and bring them back to Earth. A second option is to attach a propulsion system to the asteroid and, by means of a small manoeuvre, capture it into a suitable orbit of the Earth-Moon system. This last technique, although difficult to carry out, allows for a much simpler mining strategy once the asteroid is inside the Earth-Moon system. In this context, near Earth asteroids (NEAs) offer very suitable targets.

There are several works in the literature that analyse the capture near the L_1 and L_2 collinear points (for a recent review, see [34]). For instance, [33] studies the capture opportunities for a selection of NEAs targeting Lyapunov and Halo orbits of the Earth-Sun Circular Restricted Three-Body Problem (RTBP). The capture of NEAs targeting L_2 Lyapunov and Halo orbits

* Corresponding author.
E-mail addresses: angel@maia.ub.es (À. Jorba), bego@maia.ub.es (B. Nicolás).

https://doi.org/10.1016/j.cnsns.2021.105948

in the Earth-Moon RTBP is discussed in [35]. In both works, the case of asteroid 2006 RH120 is analysed, resulting in costs between 58 m/s and 298 m/s in the first case (Earth-Sun RTBP) and less than 500 m/s in the second (Earth-Moon RTBP). The attention paid to the collinear points L_1 and L_2 is due to their strong instability and low energy level, that aids to a rapid dynamics to enter and leave the system passing close to the small primary, either the Moon in the Earth-Moon system or the Earth in the Sun-Earth system. However this advantage to have a fast approach is also a disadvantage to control it, since high fuel costs have to be employed to avoid the asteroid to leave this region with the same facility as it is approached. Not to mention the risks of a crash into the Moon or the Earth. Other works suggest the capture of an asteroid without targeting any particular orbit, for example, in [36], the authors analyse the lengthening of the time that the asteroid 2006 RH120 was orbiting the Earth in its last approach in 2006, by sweeping a three dimensional mesh on the parameters that define a low thrust maneouver. Among their results, a manouver of total Δv of only 32 m/s is found to have been able to extend this time another five years.

In this paper we propose the neighbourhood of the L_3 point of the Earth-Moon system as one of the potential destinations for a captured asteroid. One of the advantages of this region is a very mild instability that allows for an extremely cheap control to keep the asteroid there: the station keeping manoeuvres to remain in the neighbourhood of L_3 are of just some cm/s per year [11]. So, it is very cheap to keep the asteroid in that region, in order to perform a mining process or just waiting for the right moment to send it towards to some other region. Another advantage of this region is that, as we will see later on, there are invariant manifolds connecting the vicinity of L_3 with the trajectories of some NEAs.

The model we have used is the planar Bicircular model. In this model, Earth and Moon revolve in circular orbits around their centre of mass, and this centre of mass and the Sun revolve in circular orbit around the (Earth+Moon)-Sun centre of mass. The description of the motion of a fourth infinitesimal particle moving under the gravitational attraction of these three masses is known as the Bicircular problem (BCP). The BCP is usually written as a periodic time-dependent perturbation of the RTBP, where the time dependence comes from the presence of the Sun. In this model, when the infinitesimal particle is at some distance from Earth and Moon it follows a nearly-Keplerian orbit around the Sun, while when enters the Earth-Moon systems it follows the dynamics of a Restricted Three-Body Problem with a perturbation coming from the Sun. Hence, it seems a natural initial model to study the capture of a NEA.

It is well-known that the L_3 point of the RTBP becomes a periodic orbit in the BCP model of centre$\times$saddle type. It is also well known that, under generic conditions, the elliptic directions of such a periodic orbit give rise to a one-parametric family of quasi-periodic motions (invariant tori) with two basic frequencies, one coming from the effect of the Sun and one coming from the family of periodic Lyapunov orbits of L_3 in the Earth-Moon RTBP [25,26]. If we use the temporal Poincaré map given by the period of the Sun these quasi-periodic orbits become an invariant curve. The computation of these invariant tori is done on a suitable Poincaré map and it is discussed in [21]. These invariant curves are (mildly) hyperbolic so that they have stable/unstable invariant manifolds. A standard procedure to compute these manifolds is to use the linear approximation to the manifolds and globalising them by numerical integration. In this case, to have a good level of accuracy the numerical integrations have to start very close to the torus and, hence, a long integration time is needed to move away from the neighbourhood of L_3. This long integration time introduces some numerical difficulties (see Section 4) and, for this reason, we have implemented the parametrization method to compute these invariant manifolds up to high order. As these computations are done in a Poincaré map, the parametrization method is combined by a jet transport technique to propagate the high order derivatives needed in the parametrization method [13]. The last step of the process is to refine trajectories on the stable manifold that arrive at some given position at a given time; the position and time of the asteroid. The difference in their velocities gives the value of the impulse maneouver, Δv, required to insert the NEA into the stable manifold.

As a test example, we have considered the capture of the asteroid 2006 RH120. This is a small asteroid (3.3 ± 0.4 meters in size [28]) that makes close approaches to the Earth-Moon system. In fact, it was orbiting the Earth from September 2006 to June 2007. We have selected the 2006 approach to show a strategy to capture it near the L_3 point of the Earth-Moon system. We show that there are many options to capture it using a Δv in the range 100-300 m/s, and some other options to capture it with a Δv below 100 m/s. Remarkably, there is one option with a Δv as low as 20 m/s.

The paper is structured as follows. Section 2 describes the BCP model and some previous results that will be used here, Section 3 explains the computation of invariant manifolds of invariant curves, Section 4 discusses the use of these manifolds to construct a capturing strategy, and Section 5 shows the results of applying the previous strategy to the capture of the asteroid 2006 RH120. Finally, Section 6 is devoted to the conclusions and future work.

2. The Bicircular model

The Bicircular Problem (BCP) can be seen as a modification of the Circular Restricted Three Body Problem (RTBP), in which the effect of the gravitational field of a fourth body is introduced as a time-periodic perturbation [9,18]. We consider the primaries to be the Earth and the Moon, and the perturbative body to be the Sun. As in the RTBP, units are taken such that the distance between Earth and Moon (3.8440×10^5 km) and the sum of their masses (6.0457×10^{24} kg) are normalised to 1, and such that their period (27.321577 days) is normalised to 2π. In these units the gravitational constant is 1. Considering the synodic Earth-Moon RTBP frame of reference with the origin fixed at the Earth-Moon barycentre, the

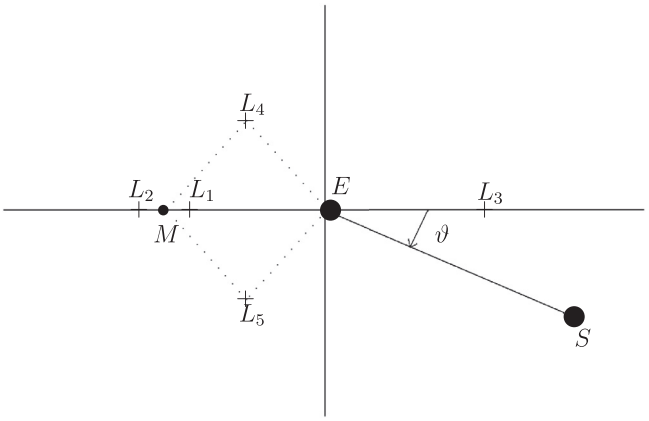

Fig. 1. Schematic of the Bicircular Model. Note that distance to Sun is not in scale.

Table 1
Parameters of the Bicircular model for the Earth-Moon system, in RTBP units.

μ	m_s	ω_s	a_s
0.012150582	328900.55	0.925195985	388.811143023

Earth placed at $(\mu, 0)$ and the Moon at $(-1+\mu, 0)$, see Fig. 1, the Hamiltonian for the planar BCP is written as

$$H_{BCP} = \frac{1}{2}(p_x^2 + p_y^2) + yp_x - xp_y - \frac{1-\mu}{r_{PE}} - \frac{\mu}{r_{PM}} - \frac{m_s}{r_{PS}} - \frac{m_s}{a_s^2}(y\sin\vartheta - x\cos\vartheta), \tag{1}$$

being (x, y, p_x, p_y) the positions and momenta of the particle, such that $r_{PE} = ((x-\mu)^2 + y^2)^{1/2}$, $r_{PM} = ((x-\mu+1)^2 + y^2)^{1/2}$ and $r_{PS} = ((x - a_s\cos\vartheta)^2 + (y + a_s\sin\vartheta)^2)^{1/2}$ are the distances from Earth, Moon and Sun to the particle, respectively. m_s is the mass of the Sun, a_s is the distance between the Sun and the Earth-Moon barycentre, and $\vartheta = \omega_s t$ is the angle that specifies the position of the Sun at each time t, where ω_s is the Sun angular velocity with respect to the Earth-Moon system, see Fig. 1. In this system, the period of the Sun, $T = 2\pi/\omega_s \approx 29.53$ days, coincides with the synodic period of the Moon.

Notice that, the Hamiltonian in (1) is the Hamiltonian of the RTBP plus the last two terms that account for the solar gravity perturbation. To justify that the effect of the Sun is small, let us note that if we expand the potential of the Sun at the Earth-Moon barycentre ($x = y = 0$), the first order term cancels with the Coriolis term $m_s(y\sin\vartheta - x\cos\vartheta)/a_s^2$ so that the contribution due to the gravity of the Sun starts at second order with the coefficient m_s/a_s^3 which makes its contribution small (in fact, in [20] it is shown that the radiation pressure on a Solar sail in the Earth-Moon system is higher than the gravitational effect of the Sun on the sail). In Table 1 the parameters for Earth-Moon-Sun BCP are presented in adimensional units. Notice that in this reference frame, the Sun is seen as rotating around the Earth-Moon barycentre. Notice that in the BCP, the gravitational attraction of the Sun affects the particle, and not to the primaries. Nevertheless, BCP has been proved to describe dynamical phenomena in the Earth-Moon system through comparison with real system integrations, [21,22,32].

Under generic conditions, the equilibrium points of the RTBP are replaced by periodic orbits in the BCP, with the period of the perturbation. In particular, for the Earth-Moon system under solar perturbation, each of the three collinear points, L_1, L_2 and L_3, are replaced by one unstable periodic orbit[1] and the triangular equilibrium points, L_4 and L_5 (that are linearly stable in the RTBP) are replaced by three periodic orbits; two of them stable and the other one, linearly unstable, see [22,32].

2.1. The Lyapunov family of quasi-periodic orbits near L_3

The periodic orbit of the BCP replacing the L_3 point of the RTBP is of centre×saddle type. Therefore, under generic hypothesis, there exists a Cantor family of quasi-periodic orbits emanating from its centre direction [25,26]. The fact that the family is Cantorian means that there is an infinite number of holes in the family. These holes correspond to resonances and are exponentially small with the order of the resonance [26]. This implies that only a few of them are visible, corresponding to low order resonances. The resonances here are all of high order and this makes that, with the usual double precision accuracy, the family looks like if it were continuous. The family of quasi-periodic solutions around L_3 have two basic frequencies (the frequency of the Sun in the BCP plus a frequency coming from the centre direction of the periodic orbit) and inherit the hyperbolic character of the periodic orbit. Next, we summarise the computation of this family of quasi-periodic motions and their linear stability (for more details, see [21]).

[1] The L_2 point is a bit more involved, see [5,19,31]

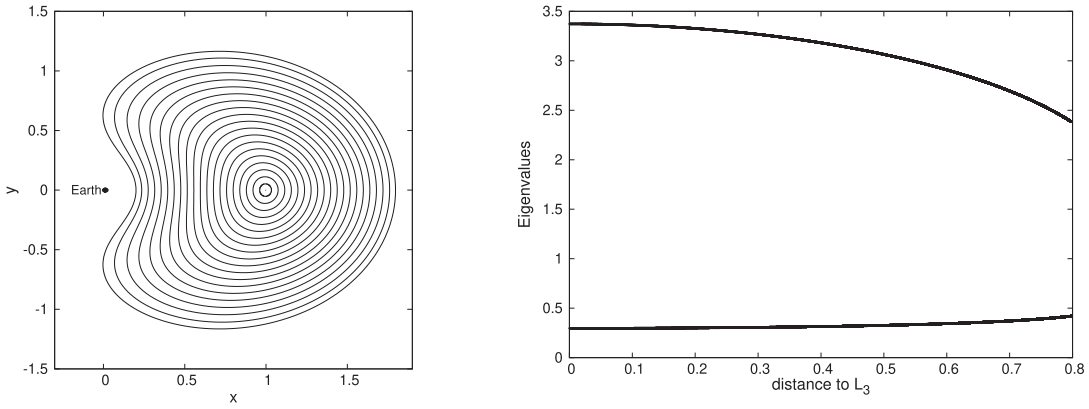

Fig. 2. Left: the family of invariant curves around L_3 projected in XY-plane; the Earth is included as a black circle of corresponding radius. Right: hyperbolic eigenvalues of the invariant curves according to their distance to the periodic orbit replacing L_3.

As the time dependence of the Hamiltonian is periodic, we use the Poincaré map P defined with the period T of this time dependence. This is a 4D discrete autonomous dynamical system whose fixed points correspond to periodic orbits of period T of the Hamiltonian. In the same way, the above-mentioned quasi-periodic orbits become invariant curves for this map. An invariant curve can be represented by a smooth map $\varphi : \mathbb{T}^1 \to \mathbb{R}^4$ that satisfies an invariance condition,

$$P(\varphi(\theta)) = \varphi(\theta + \omega), \qquad \forall \theta \in \mathbb{T}^1, \tag{2}$$

where $\omega \in \mathbb{T}^1$ is the frequency of the invariant curve. To approximate invariant curves, we represent them by truncated Fourier series and we apply a Newton method to find the Fourier coefficients that solve the invariance equation (2). The number of Fourier coefficients is selected according to the accuracy requirements. Once the invariant curve is computed, its stability is obtained from the following generalised eigenvalue problem,

$$D_x P(\varphi(\theta))\psi(\theta) = \lambda \Gamma_\omega \psi(\theta), \tag{3}$$

where Γ_ω denotes the operator $\Gamma_\omega : C(\mathbb{T}^1, \mathbb{C}^4) \to C(\mathbb{T}^1, \mathbb{C}^4)$ such that $\Gamma_\omega \psi(\theta) = \psi(\theta + \omega)$. As before, this eigenproblem is solved in the space of Fourier coefficients. Following [23] it is not difficult to see that it has 4 distinguished eigenvalues: a couple of 1 (a 1 refers to the tangent direction to the invariant curve and a 1 refers to the tangent direction to the family of invariant curves), and a real couple λ_u, $\lambda_s = \lambda_u^{-1}$ with, say, $|\lambda_u| > 1$. Then, the eigenfunctions of eigenvalues λ_u and λ_s give the linear approximation to the unstable and stable manifolds: for instance, if φ is the invariant curve, and ψ the stable eigenfunction, then

$$(\theta, \sigma) \mapsto \varphi(\theta) + \psi(\theta)\sigma, \quad (\theta, \sigma) \in \mathbb{T}^1 \times \mathbb{R}, \tag{4}$$

is the linear approximation to the stable manifold. Of course, this approximation is accurate only for small values of $|\sigma|$.

Fig. 2 (left) shows the family of invariant curves that emanates from the centre direction of the periodic orbit that replaces L_3 in the BCP model. This family and its stability has already been computed in [21]. Fig. 2 (right) shows the eigenvalues λ_s and λ_u. The horizontal axis identifies the invariant curves by their distance to the periodic orbit replacing L_3. This distance is defined as follows. The periodic orbit that replaces L_3 is seen as a fixed point p_0 of the map P. Due to the symmetries of this problem, it happens that p_0 is on the OX axis. On the other hand, the parametrization of the invariant curves, $\theta \mapsto \varphi(\theta)$, has been chosen such that $\varphi(0)$ is on the OX axis and to the left of p_0. Then, the distance between the curves and the periodic orbit is defined as the distance, on the OX axis, between the points p_0 and $\varphi(0)$. This distance is what we have called "distance to L_3", for short.

3. Invariant manifolds of invariant curves

In this section we focus on the effective computation a high order approximation to the invariant manifolds of an invariant curve. We will use the well-known parametrization method, that has been used for numerical computations in the 80's by C. Simó to approximate the invariant manifolds of equilibrium points of ODEs and fixed points of maps (see also [10]), but it is remarkable that this method is also an excellent tool to prove the existence of invariant manifolds, as shown in [7]. A very good exposition can be found in the book [16]. The case of the stable/unstable manifolds of an invariant curve of quasi-periodic maps is considered in [17]. In this paper, we combine the parametrization method with the jet transport technique to compute accurate high order approximation of stable/unstable manifolds of invariant curves of Poincaré maps.

3.1. Jet transport

Jet transport is a computational technique to compute high order derivatives of the flow of an ODE with respect to initial data and/or parameters [2–4,6,38]. It is based on using automatic differentiation [15] on a numerical integration of ODEs. The main idea is to replace the basic arithmetic of the integrator by an arithmetic of (truncated) formal power series in several variables. The formal power series codifies the value of a function (the constant term) and their derivatives (the coefficients of each monomial), and the propagation of these power series through the numerical integration produces exactly the same results as the integration of the corresponding high order variational equations of the ODE [13]. Although other options are possible, here we have used, as basic numerical integrator, the Taylor method [27] that has been modified to operate on power series, see [13].

3.2. The parametrization method

Let us describe the procedure with some level of detail for our situation. First, let us write a formal Taylor-Fourier expansion of the invariant manifold depending on two parameters, $\theta \in \mathbb{T}^1$ and $\sigma \in \mathbb{R}$,

$$W(\theta,\sigma) = a_0(\theta) + a_1(\theta)\sigma + \sum_{k\geq 2} a_k(\theta)\sigma^k,$$

where $a_k(\theta) \in \mathbb{R}^4$. It is clear that a_0 is the parametrization of the invariant curve (φ in (4)) and a_1 the eigenfunction (ψ in (4)) and this gives the linear approximation to the invariant manifold. To compute the functions a_k, $k \geq 2$, we use that the manifold must be invariant under the Poincaré map P,

$$P(W(\theta,\sigma)) = W(\theta+\omega, \lambda\sigma), \tag{5}$$

where λ is the eigenvalue related to the eigenfunction ψ. This invariance condition can also be visualized with the help of a commutative diagram,

$$\begin{array}{ccc} \mathbb{T}^1\times]0,\infty[& \xrightarrow{\Gamma_\omega\times\Lambda} & \mathbb{T}^1\times]0,\infty[\\ \Big\downarrow W & & \Big\downarrow W \\ \mathbb{R}^4 & \xrightarrow{P} & \mathbb{R}^4 \end{array}$$

where $(\Gamma_\omega \times \Lambda)(\theta,\sigma) = (\theta+\omega, \lambda\sigma)$. It is clear that

$$W(\theta+\omega,\lambda\sigma) = a_0(\theta+\omega) + a_1(\theta+\omega)\lambda\sigma + \sum_{k\geq 2} a_k(\theta+\omega)\lambda^k\sigma^k.$$

As it is usual in these situations, we find the coefficients a_k order by order. Let us denote by W_m the truncation

$$W_m(\theta,\sigma) = a_0(\theta) + a_1(\theta)\sigma + \sum_{k=2}^{m} a_k(\theta)\sigma^k,$$

and let us assume that we know W_{m-1} and we want to compute W_m (that is, we assume we know a_0,..., a_{m-1} and we want to compute a_m). Applying the Poincaré map P to W_m,

$$\begin{aligned} P(W_m(\theta,\sigma)) &= P(W_{m-1}(\theta,\sigma)) + DP(W_{m-1}(\theta,\sigma))a_m(\theta)\sigma^m + O_{m+1}(\sigma) \\ &= P(W_{m-1}(\theta,\sigma)) + DP(a_0(\theta))a_m(\theta)\sigma^m + O_{m+1}(\sigma). \end{aligned} \tag{6}$$

As W_{m-1} is the Taylor-Fourier expansion of the invariant manifold, we have that it is invariant up to degree $m-1$, that is

$$P(W_{m-1}(\theta,\sigma)) = W_{m-1}(\theta+\omega,\lambda\sigma) + b_m(\theta)\sigma^m + O_{m+1}(\sigma),$$

where $b_m(\theta)$ denotes the coefficient at order m that appears in the evaluation up to order m of the Poincaré map of W_{m-1}. Therefore, putting this last expression into (6) we obtain

$$P(W_m(\theta,\sigma)) = W_{m-1}(\theta+\omega,\lambda\sigma) + b_m(\theta)\sigma^m + DP(a_0(\theta))a_m(\theta)\sigma^m + O_{m+1}(\sigma).$$

Next, we impose the invariance condition (5) up to degree m, to obtain

$$b_m(\theta)\sigma^m + DP(a_0(\theta))a_m(\theta)\sigma^m = a_m(\theta+\omega)\lambda^m\sigma^m,$$

which can be rewritten as

$$(DP(a_0(\theta)) - \lambda^m\Gamma_\omega)a_m(\theta) = -b_m(\theta). \tag{7}$$

This is an equation that, under generic conditions of non-resonance, uniquely determines the function a_m. The numerical treatment of this equation is discussed in the next section.

Note that this procedure is valid for parametrizing both the stable and the unstable invariant manifold of an invariant curve. However, when applying the map P forward in time to compute the stable invariant manifold the expanding effect

of the (unwanted) unstable direction amplifies the error propagation. For this reason, it is more accurate to parametrize the stable invariant manifold by imposing the invariance equation on the inverse of the Poincaré map, that can be easily obtained by integrating backward in time,

$$P^{-1}(W(\theta,\sigma)) = W(\theta-\omega, \frac{\sigma}{\lambda}). \tag{8}$$

Again, we solve (8) order by order. Obviously, as before, order 0 and order 1 correspond to the invariant curve and the associated eigenfunction, respectively. In general, assuming that we know the coefficients up to order $m-1$, coefficient $a_m(\theta)$ satisfies the system given by

$$(DP^{-1}(a_0(\theta)) - \lambda^{-m}\Gamma_{-\omega})a_m(\theta) = -b_m^-(\theta), \qquad m \geq 2, \tag{9}$$

where, as before, $b_m^-(\theta)$ denotes the coefficient at order m of the evaluation by the inverse Poincaré map of the manifold up to order $m-1$.

3.3. The numerical algorithm

We have already seen that the order zero and one coefficients, a_0 and a_1, correspond to the invariant curve and to the linear approximation to the invariant manifold, respectively, and that the coefficients of order higher than one, a_k are obtained by solving recursively the system in Eqs. (7) or (9). In this section we detail the algorithm for computing these coefficients of the parametrization of the invariant manifolds.

As it has been mentioned before, the procedures to compute the invariant curve and linear stability can be found in [8,12,23]. There, the discretization of the invariant curve is done by means of a real (truncated) Fourier series in terms of the angle $\theta \in [0, 2\pi]$,

$$\varphi(\theta) \approx \alpha_0 + \sum_{\kappa=1}^{N} \alpha_\kappa \cos(\kappa\theta) + \beta_\kappa \sin(\kappa\theta), \tag{10}$$

being $(\alpha_0, \alpha_\kappa, \beta_\kappa)$ the Fourier coefficients for the modes $\kappa \in [1, N]$. The generalised eigenvalue problem (3) is also solved in terms of the Fourier coefficients, so that eigenfunctions are also approximated by Fourier series truncated at order N.

Expressing the invariant curve and eigenfunction as Fourier series is very convenient from the point of view of computations, due to their fast convergence. Moreover, the operator Γ_ω is just a 2×2 block diagonal matrix matrix that applies a rotation equal to ω to each pair of coefficients $(\alpha_\kappa, \beta_\kappa)$. Following this idea, we solve the system in (7) in terms of the Fourier coefficients, what gives the expression for each a_k also as a Fourier series.

Then, the algorithm for computing the parametrization of the invariant manifold of an invariant curve up to order K starts by defining a mesh of angles along the curve: $\theta_j = 2\pi j/\ell$, being ℓ the number of points of the mesh such that $j \in [0, \ell]$ and $\theta_j \in [0, 2\pi]$, and to apply the jet transport to each of these points in order to obtain the values $b_k(\theta_j)$. Notice that, the jet transport algorithm applied to an invariant manifold up to order $k-1$ gives the coefficients of order equal and higher than k, but only order k is of interest at each application.

Once we have the table of values $(b_k(\theta_j), \theta_j)$, we compute the corresponding Fourier series for the $b_k(\theta)$ coefficients, and solve one linear system in terms of Fourier coefficients to find coefficients $a_k(\theta)$ as Fourier series:

$$(DP(a_0(\theta)) - \lambda^k\Gamma_\omega)a_k(\theta) = -b_k(\theta). \tag{11}$$

Note that, $b_k(\theta)$ is then parametrized by a Fourier series of $\ell = 2N+1$, Fourier coefficients, and consequently, the series for $a_k(\theta)$ has the same number of modes. For convenience, we start using the same number of modes used for discretizing the invariant curve and its eigenfunction. However, it may happen that this number, that is good enough for approximating the invariant curve and the eigenfunction, does not approximate accurately some of the $a_k(\theta)$ for $k \geq 2$, and therefore it is necessary to add modes to the Fourier series in order to improve the approximation of the invariant manifold. As the accuracy of each $a_k(\theta)$ is related to the accuracy of the corresponding $b_k(\theta)$, when we compute the Fourier series of $b_k(\theta)$ we check the Euclidean norm of its last two modes to be below some tolerance. If it is not, we re-compute the table of values $(b_k(\theta_j), \theta_j)$ for a larger number of points such that the number of modes of $b_k(\theta)$ is increased, as well as the number of modes of $a_k(\theta)$.

Let us now summarise our numerical implementation. The starting point is a truncated Fourier series that approximates the invariant curve (φ) and a truncated Fourier series that approximates the eigenfunction ψ giving the linear approximation to the manifold. Then, $a_0 = \varphi$ and $a_1 = \psi$. Moreover, we need the $(2N+1)n \times (2N+1)n$ matrix that contains the matrix flow $DP(a_0)$ (this is the same matrix that appears in the Newton method and in the stability computation (3)). As before, $2N+1$ is the number of Fourier coefficients and n the dimension of the dynamical system ($n = 4$ in our case). The chosen values of N and the accuracy is discussed later on (see also [21]).

Note that at each step we have to evaluate $P(W_m)$, where W_m is a Taylor-Fourier series. As the jet transport technique only allows to evaluate P on power series, we compute $\{W(\theta_j, \sigma)\}_j$ being θ_j a suitable equispaced mesh of values of θ. Each $W(\theta_j, \sigma)$ is now a power series so we can compute $P(W(\theta_j, \sigma))$ and, using a Fourier transform, we obtain $P(W_m)$.

To end this section, let us summarise the computation of the coefficients a_k, $k \geq 2$, which is done recurrently order by order. So, assume that we know W_{m-1} and we want to compute W_m. We also assume that we have computed and stored the matrix (of size $(2N+1)n \times (2N+1)n$) $DP(a_0(\theta))$. Then,

1. Evaluate $W_{m-1}(\theta_j, \sigma)$ on a mesh $\{\theta_j\}_{j=0}^{\ell-1}$ of ℓ points ($\theta_j = 2\pi j/\ell$, $\ell = 2N+1$), to obtain ℓ polynomials of degree $m-1$.
2. Apply the jet transport algorithm (working with polynomials of degree up to m) to each of the $W_{m-1}(\theta_j, \sigma)$ polynomials to obtain the table of values $(\theta_j, b_m(\theta_j))$ from the coefficient of degree m.
3. Apply a Fourier transformation to obtain $b_m(\theta)$. We use as an estimate of the error the size of the last terms of these Fourier coefficients. If this estimate is not small enough, we repeat steps 1 and 2 with larger value of ℓ.
4. Solve the linear system in (11) to obtain a_m, and then $W_m = W_{m-1} + a_m \sigma^m$.

These steps are applied up to the desired degree for the invariant manifold.

The previous algorithm is applied "as is" to compute the unstable manifold. For the stable manifold, to minimise the error propagation, this method is applied to the inverse map P^{-1}. The reason for this better numerical behaviour is that the stable manifold is a repelling manifold under P and not repelling under P^{-1} (and the unstable manifold is repelling under P^{-1} and not repelling under P). Moreover, note that the computation of the inverse of the Poincaré map, P^{-1}, can be done very easily by simply integrating backward in time.

3.4. Fundamental Cylinder (FC)

The stable/unstable manifolds of an invariant curve can be seen as cylinders, parametrized by the same angle as the invariant curve (θ) and a parameter to move away from the invariant curve (σ). Looking at these parameters, the dynamics on this cylinder is very simple: the point corresponding to the parameter values (θ, σ) in the unstable manifold is mapped to $(\theta + \omega, \lambda_u \sigma)$ through P, and, equivalently, the point corresponding to the parameter values (θ, σ) in the stable manifold is mapped to $(\theta - \omega, \lambda_s^{-1}\sigma)$ through P^{-1}. This means that we can define a set of the form $\theta \in \mathbb{T}^1$, $\sigma \in [\sigma_0, \lambda_u \sigma_0]$ for the unstable manifold (and $\sigma \in [\sigma_0, \lambda_s^{-1}\sigma_0]$ for the stable), which can be seen as a set that generates, under iteration of the map P (and P^{-1}), the complete manifold. We will refer to such set as Fundamental Cylinder (FC).

To simplify the discussion, let us focus on the unstable manifold. An approximation for a curve of the fundamental cylinder of the unstable manifold is given by $W_K^u(\theta, \sigma_0)$, where K is the order of the approximation and σ_0 is a sufficiently small value. If we choose this curve as the "lower part" of the cylinder, then the "upper part" is given by $W_K^u(\theta, \lambda_u \sigma_0)$. Note that neglecting the rotation of the angle for the upper curve does not affect the definition of the fundamental domain. The parametrization of the fundamental cylinder for the unstable invariant manifold, $W_K^u(\theta, \sigma) = \sum_{k=0}^K a_k^u(\theta)\sigma^k$ such that $\sigma \in [\sigma_0, \lambda_u \sigma_0]$, is the following:

$$z(\theta, \tau) = \sum_{k=0}^{K} a_k^u(\theta)((1 + \tau(\lambda_u - 1))\sigma_0)^k, \tag{12}$$

where $\tau \in [0, 1]$ is a parameter: when $\tau = 0$, $z(\theta, \tau)$ parametrizes the lower curve, $W_K^u(\theta, \sigma_0)$, and when $\tau = 1$, it parametrizes the upper curve, $W_K^u(\theta, \lambda_u \sigma_0)$. The FC is used as starting place for the numerical integrations used to extend the manifold as much as needed. Note that the value σ_0 has to be chosen small enough such that this representation of the FC is accurate, but large enough to minimise the integration time to reach the asteroid. The choice of σ_0 is discussed in the next section.

Finally, let us mention that for the fundamental cylinder of the stable manifold, $W_K^s(\theta, \sigma) = \sum_{k=0}^K a_k^s(\theta)\sigma^k$ such that $\sigma \in [\sigma_0, \lambda_s^{-1}\sigma_0]$, we use

$$z(\theta, \tau) = \sum_{k=0}^{K} a_k^s(\theta)((1 + \tau(1/\lambda_s - 1))\sigma)^k. \tag{13}$$

Again, $z(\theta, \tau)$ parametrizes the lower curve, $W_K^s(\theta, \sigma_0)$, when $\tau = 0$, and when $\tau = 1$ it parametrizes the upper curve, $W_K^s(\theta, \lambda_s^{-1}\sigma_0)$. The globalisation is done using the inverse of the Poincaré map.

3.5. Accuracy and tests

In this section we discuss the choice of the degree K of the parametrization of the manifolds, the estimation of the domain of validity of the computed parametrization, and the tests used to check the correctness of the results. We recall that, applying the algorithm given in Section 3.3, we approximate the coefficients a_k, up to some order K, as a truncated Fourier series,

$$a_k(\theta) \approx \alpha_0 + \sum_{\kappa=1}^{N} \alpha_\kappa \cos(\kappa\theta) + \beta_\kappa \sin(\kappa\theta).$$

As a general rule, we have that the higher the degree of the parametrization K and the number of Fourier modes N, the more accurate is the approximation of the parametrization of the invariant manifold $W(\theta, \sigma) = \sum_{k=0}^K a_k(\theta)\sigma^k$. However, when K is large enough, the gain of accuracy provided by a new degree $K+1$ of the parametrization does not compensate the computational cost needed to obtain this new degree.

To fix the discussion, let us focus on the unstable manifold (a similar discussion is valid for the stable one), and let us also assume that the value N has already been chosen to have the required accuracy, may be depending on K (see the

discussion in Section 3.3). A fast error estimate for the truncated expansion of the manifold follows from the size of the last computed term (the one of degree K),

$$\|a_K\|_1 \, |\sigma|^K \approx \varepsilon, \qquad \|a_K\|_1 = |\alpha_0| + \sum_{\kappa=1}^{N} |\alpha_\kappa| + |\beta_\kappa|.$$

We have to choose a value $\bar{\sigma}_0 > 0$ such that the parametrization of a fundamental domain as in (12) is accurate up to $\lambda_u \bar{\sigma}_0$. Hence, from the previous formula we obtain that

$$\bar{\sigma}_0 \approx \frac{1}{\lambda_u} \left(\frac{\varepsilon}{\|a_K\|_1} \right)^{1/K}. \tag{14}$$

Therefore, given an accuracy ε, we compute the value of $\bar{\sigma}_0$ and use some $\sigma_0 \le \bar{\sigma}_0$ for computing the approximation to the FC. Notice that, in the presence of symmetries, checking only the last order of the parametrization may cause problems since it could vanish depending on its parity. In this case the last two terms of the expansion have to be used.

In order to check the final accuracy of the approximation of the invariant manifold we compare the error of the invariance condition for the parametrization of the invariant manifold, $W(\theta, \sigma)$, at a given angle θ, but at two different values of σ, say σ_1 and $\sigma_2 = \sigma_1/2$. Obviously, if the parametrization of the manifold has been computed up to order K, the truncation error depends on the power $K+1$ of the parameter σ. Then, for σ_1 we would have that

$$\epsilon_1 = |P(W_K(\theta, \sigma_1)) - W_K(\theta + \omega, \lambda\sigma_1)| \approx c\sigma_1^{K+1},$$

and for σ_2,

$$\epsilon_2 = |P(W_K(\theta, \sigma_2)) - W_K(\theta + \omega, \lambda\sigma_2)| \approx c\sigma_2^{K+1},$$

where c is a constant. The relation between the two errors is

$$\frac{\epsilon_1}{\epsilon_2} \approx \frac{\sigma_1^{K+1}}{(\frac{\sigma_1}{2})^{K+1}} \approx 2^{K+1}.$$

Therefore, we compute the quantity

$$\frac{\log(\epsilon_1/\epsilon_2)}{\log(2)},$$

and check that the result corresponds to $K+1$. This test has been passed for the manifolds used in this work.

4. Computational strategy

Some parts of the invariant manifolds of the quasi-periodic orbits near L_3 move around the Earth-Moon system, while other parts escape and orbit the Sun [21]. The main idea to capture a NEA in the vicinity of L_3 is to propagate, backward in time, the stable invariant manifold of a quasi-periodic orbit near L_3 looking for encounters in positions with the target object. The difference in velocities at this "meeting point" gives the manoeuvre to inject the NEA in the manifold so that the natural dynamics of the problem sends the asteroid to the neighbourhood of L_3. As mentioned in the Introduction, the advantages of using L_3 are mainly a very low cost for the station keeping there, the possibilities offered to reach a different region from there and the low risk of crashing during the transfer.

It is worth mentioning that a preliminary exploration of the possibilities of L_3 for the capture was done using the linear approximation of the invariant manifolds of the invariant curves shown in Fig. 2. However we do not aim just to find an invariant manifold that passes close to the position of an asteroid to justify the capture, but to be able to find the initial condition on the fundamental domain of a torus that is sent (by the backwards flow of the BCP) to the position of the asteroid at the right time. Notice that, when using the linear approximation of the invariant manifolds, the fundamental domain needs to be defined very close to the invariant curve (for $\sigma \le 10^{-5}$), therefore the globalisation of those initial conditions requires numerical integration of trajectories that spend a significant amount of time just closely following the quasi-periodic orbit, increasing the numerical errors and making more difficult to find the initial condition that corresponds exactly with the position of the asteroid. This difficulty is solved using a high order parametrization method for the invariant manifolds.

The computational strategy for the capture that we present here is based on three steps. First of all, the positions and velocities of the asteroid are obtained from the JPL Horizons system [24] in the ecliptic reference frame at some Julian epochs. Therefore, a change of positions, velocities and time[2] is needed to transfer the information on the location of the asteroid to the Bicircular model. This is done in Section 4.1. The second step is to define the fundamental domains of the stable invariant manifolds of tori around L_3, globalise them backward in time, see Section 4.2, and compare the position of the manifold with that of the asteroid. This allows to identify sets of initial conditions on the FC that approach the asteroid.

[2] We recall that the BCP is a time-dependent model.

Finally, in Section 4.3, we explain a Newton method used to compute the initial condition on the FC that arrives, backward in time, to the location (positions and time) of the asteroid.

As the BCP is a periodically time-dependent model, we can look for encounters NEA-manifolds at different times. If we use the Poincaré map P then we only look for encounters at time $t = 0 \bmod T$ (that is, after an integer number of periods of the BCP). In our analysis of the capture we define different temporal sections, corresponding to an integer number of periods, to a quarter, to a half and to three quarter of the period. This has two effects; on the one hand, the relative position with respect to the Sun changes and this can aid (or difficult) the capture, and on the other hand, the positions of the asteroid itself are also different.

Finally, we want to emphasise that this work studies, as an example, the capture of the asteroid 2006 RH120 in its last approach to the Earth, but it is easy to see that the whole strategy described here can be used to study the capture of any other asteroid of interest.

4.1. Change of coordinates and time

In order to define the change of coordinates and time for the asteroid from the ones provided by JPL (ecliptic coordinates centered at the Solar system barycentre) to BCP coordinates we make use of two facts: first, in the BCP the positions of the Earth, Moon and Sun at time 0 correspond to a lunar eclipse, so it is easy to identify a real lunar eclipse and take it as the origin for time ($t_0 = T_{ECLIPSE}$ in Julian days), the second fact is that the time is a periodic variable in this model, therefore, at every solar period the Earth, the Moon and the Sun come back to their initial positions at time 0. According to these two facts, we can establish any initial time, t_0, and take the ephemerides of the asteroid at every solar period, such that all those different Julian epochs of the asteroid correspond to the same temporal section in the BCP. Then, the positions and velocities of the asteroid are translated to the synodic reference frame of the BCP and compared with those of the invariant manifolds of invariant curves computed at the same temporal sections.

As it has been mentioned before, we analyse different temporal sections. Epochs defined as

$$t = t_0 + N_T T, \qquad \text{where } t_0 = T_{ECLIPSE} + S_T T, \qquad S_T = \left\{0, \frac{1}{4}, \frac{1}{2}, \frac{3}{4}\right\},$$

being t_0 the origin of time, T the solar period, N_T an integer number of solar periods and S_T a fraction defines the temporal sections; for $S_T = 0$ the epochs correspond to times 0 or "$N_T T$" (integer number of periods) in the BCP, for $S_T = \frac{1}{4}$ epochs correspond to temporal section at a quarter of the period, for $S_T = \frac{1}{2}$ to a half of the period and for $S_T = \frac{3}{4}$ to three quarter of the period.

Since $T = \frac{2\pi}{\omega_s}$ in RTBP units, $T = \frac{2\pi}{\omega_s}\frac{27.321577}{2\pi}$ in days, the Julian epochs of interest for the asteroid are those such that

$$t = t_0 + N_T \frac{27.321577}{\omega_s} \qquad \text{where } t_0 = T_{ECLIPSE} + S_T \frac{27.321577}{\omega_s}, \qquad S_T = \left\{0, \frac{1}{4}, \frac{1}{2}, \frac{3}{4}\right\}. \tag{15}$$

Once we select suitable epochs, JPL Horizons database is used to obtain the positions and velocities of the asteroid in the ecliptic's plane at those specific times. A change of coordinates needs to be applied to them for their analysis in the Bicircular Problem. In [14,21], the change of coordinates to translate a position in the adimensional synodical reference frame to the ecliptic one is explained, so let us only summarise it here. Let e be the positions of the asteroid in the ecliptic frame and a its positions on the adimensional BCP system; e and a are related by an orthogonal matrix C to change from rotating to non-rotating frame, by a scale factor $k = ||R_E - R_M||$ to correct the length unit and by a translation to move the origin from the Earth-Moon barycentre b to the barycentre of the solar system,

$$e = kCa + b. \tag{16}$$

Matrix C is composed by three unitary column vectors,

$$c_1 = \frac{R_E - R_M}{||R_E - R_M||}, \qquad c_3 = \frac{(R_M - R_E) \wedge (V_M - V_E)}{||(R_M - R_E) \wedge (V_M - V_E)||}, \qquad c_2 = c_3 \wedge c_1,$$

where R_E, R_M, V_E and V_M are the positions and the velocities of the Earth and Moon in the ecliptic frame.

Three observations need to be done. First one, in order to translate velocities between the two systems, it is necessary to derive (16) with respect to time, what involves the accelerations of the Earth and the Moon. Second one, as we want to translate the positions provided by the JPL database to the BCP frame, we have to apply the inverse change of coordinates. This requires the inverse of matrix C, that does not suppose any difficulty since it is orthogonal. And the last one, since we consider the planar BCP, we project the positions a and their velocities to the XY-plane.

In our example, we study the cost to capture the asteroid 2006 RH120 near L_3. This NEA was naturally captured by the Earth from September 2006 to June 2007. We analyse the possibilities of capture at different epochs that verify (15), such that all these epochs correspond to the same temporal section in the BCP for a given S_T. The selected epochs go from April 2006 and May 2007, some months before and along the time of the natural capture. The reasons for choosing this time span are the following: at these epochs the vertical coordinate is lower than in previous epochs, the change of coordinates (16) is more precise close to (or inside) the Earth-Moon system, and finally, considering positions close to the system, the propagation time of the invariant manifolds is quite low, so that we can guarantee a certain level of control on the numerical errors.

Table 2
Fifteen epochs corresponding to time 0 or $N_T T$ in the BCP, and the coordinates of the asteroid 2006 RH120 in the planar BCP at these epochs.

it	Epoch (Julian Day)	x	y	p_x	p_y
1	2453838.552774182 (2006-Apr-13)	8.49569856e+00	5.32382756e+00	-1.32303889e+00	6.39230591e-01
2	2453868.083357353 (2006-May-12)	4.30485868e+00	2.69869849e+00	-5.98173604e-01	4.69696447e-01
3	2453897.613940524 (2006-Jun-11)	2.20409179e+00	3.15215977e+00	-2.31495071e-01	4.09922742e-01
4	2453927.144523695 (2006-Jul-10)	1.79617205e+00	3.52278287e+00	4.88502390e-02	5.27242305e-02
5	2453956.675106866 (2006-Aug-09)	8.44580321e-01	1.94256864e+00	-1.83258282e-01	-2.87989646e-01
6	2453986.205690037 (2006-Sep-07)	-2.03317473e+00	3.96100179e-01	-3.27669077e-01	3.32987066e-02
7	2454015.736273209 (2006-Oct-07)	-1.77595242e+00	-6.00168179e-01	1.34571469e-01	-5.87429182e-02
8	2454045.266856380 (2006-Nov-05)	-1.59983939e+00	-1.84351841e+00	-1.29626305e-01	1.68008169e-02
9	2454074.797439550 (2006-Dec-05)	-2.52446813e+00	-1.45236080e+00	4.97133752e-02	2.81586255e-01
10	2454104.328022720 (2007-Jan-03)	5.36966985e-01	1.89106392e-01	9.19935708e-01	-1.16359612e-01
11	2454133.858605890 (2007-Feb-02)	1.01383428e+00	-1.06799662e+00	-2.12516151e-01	1.87709985e-01
12	2454163.389189060 (2007-Mar-03)	-5.50357733e-01	4.66104142e-01	-1.47342869e-01	2.34743158e-01
13	2454192.919772240 (2007-Apr-02)	1.55999311e-01	-1.47760228e+00	1.76720970e-01	-6.54112731e-01
14	2454222.450355410 (2007-May-01)	-1.05304516e+00	-1.90933922e+00	1.94206705e-01	1.00575691e-01
15	2454251.980938580 (2007-May-31)	-3.67319092e-01	5.92231168e-01	2.52078533e-01	2.49872133e-01

The exact epochs and coordinates of the asteroid in the planar BCP at a temporal section corresponding to integer number of solar periods ($S_T = 0$ in (15) and taking $T_{ECLIPSE} = 2451564.69787$ Julian Days) for the selected time span, are shown in Table 2. First column designates an identity number to each epoch.

4.2. Invariant manifolds

The Bicircular Problem, as many other classical mechanical systems, presents a symmetry when inverting the time; if $(x(t), y(t), p_x(t), p_y(t), t)$ is a particular solution of the system, also is $(x(t), -y(t), -p_x(t), p_y(t), -t)$. Since the computed invariant curves near L_3 cut symmetrically the OX axis, they are symmetric to themselves (self-symmetric), and their stable and unstable manifolds associated are also symmetric between them. Also, in our frame of the BCP, $\lambda_u = \lambda_s^{-1}$ due to the Hamiltonian structure. Therefore, we can compute only one invariant manifold (either the stable or the unstable) and have both, since

$$W^s(\theta, \sigma)\{x, y, p_x, p_y\} = W^u(\theta, \sigma)\{x, -y, -p_x, p_y\}.$$

In this work we have computed the unstable manifolds and we have used the symmetry to obtain the stable one.

The family of invariant curves around L_3 covers a wide area of the Earth-Moon system, see Fig. 2. However, not all of them are of interest for our application, since the outermost curves are too big and too close to the Earth. Therefore we focus on those at a maximum distance of 0.65 adimensional units from L_3. Within this distance the parametrization method is applied to a subset of curves separately by, approximately, 10^{-3} adimensional length units, to obtain a total of 614 invariant curves.

We have followed the algorithm in Section 3.3 to compute the parametrization of the invariant manifolds of these 614 invariant curves up to order $K = 16$. Looking at Fig. 2 it is clear that each invariant curve in the family has different shape and different eigenvalues as their distance to L_3 increases. This is is why each of them is discretized by a different number of Fourier modes. Moreover, the number of Fourier modes is not kept constant during the computation of the manifold: as it has been explained in Section 3.3, the number of modes is increased from one order of the parametrization to the next when needed. Notice that each order of the parametrization, m, is computed tentatively with the same number of Fourier modes as the coefficient of the previous order, $m - 1$. The criteria we have followed to increase this number is for the Euclidean norm of the last two terms of b_m to be below some tolerance that also depends on the order of the parametrization, being $tol_2 = 10^{-10}$ at order 2 and $tol_m = 2tol_{m-1}$ for $m > 2$. When this tolerance is reached, the number of modes is increased by 20. The reason for this criteria is that the requirement of accuracy can be decreased for higher order terms without loss of accuracy for the manifold. The full computation of the parametrizations of the invariant manifolds for the 614 invariant curves following the procedure explained here takes less than 1.5 hours in a computer with 16 processors.

Table 3 shows the number of Fourier modes for the coefficients of the parametrization at order 0, $N_{\kappa=0}$ (the invariant curve), and the number of modes needed for the coefficient at order 16, $N_{\kappa=16}$, for curves at different distances from L_3 in order to illustrate how the size of the discretizing series increases according to the shape of the invariant curve and to the degree of the parametrization.

Once we have the parametrizations of the stable invariant manifolds for the computed curves, we check up to which distance from the invariant curve each of the parametrizations can be trusted. Following the criteria defined by (14) in the Section 3.5, for the parametrizations to satisfy an error ε below 10^{-14}, the values of σ must be between 1.34×10^{-1} for the inner invariant curves of the family to 3.86×10^{-2} for the outer ones, see Table 3. This supposes a big improvement with respect to the value $\sigma \approx 10^{-5}$ needed for the linear approximation.

Table 3
Values of the unstable eigenvalue (λ_u), the number of Fourier modes needed for the orders of the parametrizations 0 ($N_{\kappa=0}$) and 16 ($N_{\kappa=16}$) and the σ parameter such that the error of the parametrization up to order $K = 16$ is below 10^{-14}, for invariant curves at different distances from L_3.

distance to L_3	λ_u	$N_{\kappa=0}$	$N_{\kappa=16}$	$\bar{\sigma}_0$ from (14)
10^{-3}	3.37281360	25	25	1.34E-01
0.1	3.36135224	27	27	9.28E-02
0.2	3.32665559	28	48	7.20E-02
0.3	3.26751807	29	69	5.86E-02
0.4	3.18166131	32	92	5.02E-02
0.5	3.06474188	45	125	4.45E-02
0.6	2.90843912	72	332	4.04E-02
0.65	2.79811097	84	424	3.86E-02

Table 4
Values of σ and the number of divisions taken for the mesh of (θ, τ) to define the fundamental cylinders for the invariant curves depending on their distance to L_3.

distances to L_3	$\lvert\sigma\rvert$ considered	divisions in θ	divisions in τ
10^{-3} - 0.1	5.00E-02	1000	500
0.1 - 0.3	5.00E-02	2000	500
0.3 - 0.4	5.00E-02	2500	400
0.4 - 0.65	2.50E-02	5000	200

Now we have the information needed to define fundamental domains for the stable invariant manifolds (13), as explained in Section 3.4. These domains are cylinder shaped and they are parametrized by two parameters, θ and τ,

$$(\theta, \tau) \in [0, 2\pi] \times [0, 1] \mapsto z(\theta, \tau) = \sum_{k=0}^{K} a_k^s(\theta)((1 + \tau(1/\lambda_s - 1))\sigma)^k.$$

Notice that σ may have positive or negative values, in order to parametrize the two branches of the stable invariant manifold. Therefore, to analyse the fundamental domains, first, we need to specify a value for σ and to make a mesh on the two parameters, such that every point in the fundamental cylinder, (θ, τ), is an initial condition on the stable invariant manifold. For each invariant curve we need to specify the value of σ and of the number of divisions taken along the angle θ and in parameter τ to define the mesh of its fundamental cylinder. The selected values are taken attending to the differences observed between the parametrizations of the manifolds for curves at different distances to L_3. Table 4 collects the values considered depending on the range of distance at which the curve is placed. This way, the mean distance between each two points in the mesh of any of the FC is of the order of 5×10^{-4} adimensional units, around 200 km.

Each of the points in the mesh, i.e. initial condition on the FC, is integrated backward in time for a maximum of 15 solar periods, by means of a Taylor method [27]. After each period of the BCP, we compute the distance to each of the fifteen positions of the asteroid given in Table 2 and we store the minimum of this distance, jointly with the differences in velocities between the point of minimum distance and the asteroid (we will refer to this difference as Δv).

If, during the integration, a trajectory in the stable manifold crashes with the Earth or the Moon the integration is stopped and we keep the information of the closest approach to the asteroid before the crash. We also compute the growth of the derivative of the trajectory w.r.t. the initial condition (this is the typical computation done to estimate Lyapunov exponents) to have an idea of the error propagation due to the instabilities of the problem. If this factor grows more than 10^9, we proceed as in the crash case, in order to discard those trajectories with significant error accumulated.

4.3. Refining an initial condition on the FC

In this section we present a Newton method to refine an initial condition on the FC, identified by two values θ and τ, that arrives to the position of the asteroid, at a specific time. The seed for the Newton method is given by the first approximation obtained in the previous section. The FC is parametrized according to (13) as

$$z(\theta, \tau) = \sum_{k}^{K} a_k^s(\theta)((1 + \tau(\lambda_s^{-1} - 1))\sigma)^k,$$

where $z(\theta, \tau)$ is a four-dimensional vector, ($z = \{x, y, p_x, p_y\}$). Therefore, what we want is to find parameters (θ, τ) such that the trajectory starting at this point reaches, at some time t_f, the position of the asteroid. This condition is written as

$$F(\theta, \tau) = \{x(\theta, \tau), y(\theta, \tau)\}_{t_f} - \{x_{asteroid}, y_{asteroid}\} = 0.$$

This is the equation we will solve using a Newton method. The derivatives of F with respect to θ and to τ follows from the chain rule,

$$\frac{\partial F}{\partial \theta}(\theta,\tau) = Df(z(\theta,\tau))_{t_f} \sum_{k=0}^{K} \frac{\partial a_k^s(\theta)}{\partial \theta}\Big[\sigma(1+\tau(\lambda_s^{-1}-1))\Big]^k,$$

$$\frac{\partial F}{\partial \tau}(\theta,\tau) = Df(z(\theta,\tau))_{t_f} \sum_{k=0}^{K} a_k^s(\theta)\sigma^k k[1+\tau(\lambda_s^{-1}-1)]^{k-1}(\lambda_s^{-1}-1),$$

being $Df(z(\theta,\tau))_{t_f}$ a 4×4 matrix that contains the derivative of the flow at the final time. Notice that for $k=0$, the derivative of $F(\theta,\tau)$ w.r.t. τ is zero, since at this order, the parametrization corresponds just to the invariant curve, that does not depend on τ. Note that these expressions involve four dimensions, but we are only interested on the first two components, since we want to refine the values of (θ,τ) that give the desired values for the (x,y) coordinates at the final time.

5. Results for the asteroid 2006 RH120

The strategy explained in the previous section has been applied to four different temporal sections, that is four Poincaré maps defined at times corresponding to an integer number of solar periods (T), to a quarter ($T/4$), to a half ($T/2$) and to three quarter ($3T/4$) of solar periods.

In the time span considered, we have found several trajectories that approach different positions of the asteroid, and requiring a low Δv for the capture at any of the four temporal sections. Since we want to compute the trajectory in the stable manifold that arrives exactly to the position of the asteroid at the right time, we look for areas in the fundamental domain of the invariant curves that show clearly a minimum of the distance to the position of the asteroid, what we have called "minimum distance areas" for short.

In order to visualise the results of globalising the invariant manifolds, we make use of colour maps corresponding to fundamental cylinders, such that the horizontal axis corresponds to $\theta \in [0, 2\pi]$, the vertical one to $\tau \in [0,1]$. Therefore, every point $(\theta,\ \tau)$ is an initial condition on the FC, that is integrated backward in time and coloured according to some magnitude. Details about the meshes used and how to compute these trajectories in the stable manifolds are presented in Section 4.2.

Each point of the FC is coloured according to the minimum distance of the trajectory starting at this point to the asteroid, making easy to identify sets of trajectories, covering some area of the FC, that approach significantly the asteroid. In order to reduce the possibilities to the most convenient ones, we add two restrictions for the coloured maps. The first one is regarding to the distance to the asteroid and the second one to the maximum affordable Δv. Only trajectories that get closer than 10^5 km to the asteroid with a difference in velocities below 1 km/s, are included in the maps. Note that these are not strong restrictions, the reason for them is only to make easy to recognise the minimum distance areas and to have an idea of the Δv that may be involved. Actually, between all the suitable trajectories that have been found, only some of those requiring a Δv below 500 m/s are presented. Also, once the minimum distance areas are identified, we use the method explained in Section 4.3 to refine a trajectory nearby that arrives to the asteroid position. The accuracy imposed to the Newton method is for the trajectory in the manifold to lay as close as 10^{-10} adimensional units (≈ 3.8 cm) to the asteroid position at the right time; this tolerance is achieved with just three or four Newton iterations.

The way to present and interpret the results is the same for any of the temporal sections, so an extended examination of the results corresponding to the temporal section at times "0" or $N_T T$ are first given in Section 5.1, and some of the results for the other three temporal sections are collected, in a more schematic way, in Section 5.2.

At the end of Section 5.1, we also give a brief explanation about the continuity in time of the minimum distance areas, and its effect on the Δv, in order to express the robustness of the trajectories susceptible to be used for the capture and to point out the possibility of implementing optimisation algorithms.

5.1. Temporal Poincaré sections at time T

The first results show that stable invariant manifolds of tori close to L_3 (that are also the most unstable ones) reach the positions of the NEA before the asteroid enters the Earth-Moon system (epochs it=1, 2 and 3 of the Table 2), with a low difference in velocities. Once the asteroid has entered the Earth-Moon system there are many initial conditions that approach the asteroid, specially for stable invariant manifolds of tori in the middle of the family, not very close to L_3, however, the difference in velocities when the asteroid is in the region close to the Earth and Moon is higher than when the asteroid is far away from any massive body, as expected according to some results found in the literature [33,35]. Finally, when the asteroid is leaving the system, the stable manifolds reach its position with a smaller difference in the velocities than when it is inside. In order to support these comments, three epochs are analysed in detail; it=2, it=7, and it=14. Since the procedure to obtain and present the results is the same for the three cases, we give a more detailed explanation for the first one, and limit ourselves to a brief version for the other two, again to avoid being repetitive.

it=2, (2006-May-12)

In Fig. 3, colour maps of the FC of different tori, covering distances to L_3 from 0.01257 to 0.05784 (a length of $\sim$ 17400.33 km) are shown. The first six maps, in the first two rows, are coloured according to the minimum distance, in km, reached between the trajectory in the stable manifold and the position of the asteroid at epoch it=2. Belonging the first colour map to the invariant curve that is closer to L_3 and the following ones, to invariant curves increasingly further away from L_3. The last six maps in Fig. 3 correspond to the same fundamental cylinders as the first two rows, this time coloured according to the instantaneous Δv in km/s, needed for the insertion of the asteroid in those trajectories belonging to stable manifolds. Remember that only trajectories that approach that position at least at 10^5 km and require a Δv of less than 1 km/s are included in the maps.

Recalling the effective continuity of the family of quasi-periodic orbits, we can compute any invariant curve between those shown in Fig. 3 and observe a similar dynamics for the invariant manifolds than that of their neighbour curves, including presenting similar minimum distance areas. Altogether, considering the union of all these tori that present some clear zones of minimum distance, there exists some three dimensional regions of significant size where there are points that allow the capture of the asteroid with a single manoeuvre.

Now, we analyse the maps in Fig. 3 separately. It is clear that for the first FC, two minimum distance areas are identified, very close one to the other, for values of θ between 3 and 4, and for some τ around 0.6. Let us call the minimum distance area on the left Minimum 1, and Minimum 2 to the one on the right. We can see these two minimum distance areas on the FC of the manifolds of nearby invariant curves that are further away from L_3. These minima start moving away and two other minimum distance areas appear for the FC in the second colour maps, named Minimum 3 (the one on the left) and 4 (the one of the right). For the FC in the third map of the first row another two minima are already found, Minimum 5 and 6. In the following maps these six minima can be easily identified. Looking at same maps in last two rows of Fig. 3, it is clear that these minimum distance areas correspond to low values of Δv. It is worth mentioning that these maps are very similar for epochs it=1 and it=3.

For each of the six minimum distance areas, and for different tori, we have computed the trajectory that exactly arrives to the asteroid position at epoch it=2, with the Newton method introduced in Section 4.3. Table 5 collects the results for the initial condition in the fundamental cylinder, θ and τ, along with the number of solar periods, N_T, that this trajectory needs to reach the position of the asteroid and the amount of Δv required for the transfer. The trajectories in the stable manifold that reach the asteroid corresponding to the first bigger two minima need five solar periods to reach the position of interest and the Δv to take advantage of their dynamics is around 254 m/s. For the next two minima, smaller in size than the previous ones, six solar periods are required and the Δv is of less than 115 m/s. Finally, for the last two, even smaller in size, another extra solar period is needed in the propagation of the trajectories and the costs are of less than 132 m/s.

Now, we perform the simulation of the capture of asteroid 2006 RH120. For this, we consider as starting point the coordinates of the asteroid at epoch it=2, add the corresponding velocity impulse, the Δv included in the Table 5, and integrate forward in time in the planar BCP, making sure that the asteroid is trapped by the stable invariant manifolds of L_3, and lead to the neighbourhood of L_3, where it remains, just spinning around the corresponding torus for long time.

In Fig. 4, we show the trajectories corresponding to the six minima present in the fifth colour map of Fig. 3. It is clear that the trajectories of the first two minima almost overlap, specially when they are far from the Earth-Moon system. Similar effect is observed with the trajectories of the second two minima, and with the ones of the third two minima. It is clear also the reason for the different values of the number of solar periods needed for each of the trajectories. Finally, these trajectories do not approach much neither of the massive bodies, although they pass at a distance of less than sixty thousand kilometres from the Moon, which makes that the norm of the derivative of the actual position w.r.t. the initial conditions be in the range between 10^3 and 10^4. This is a moderate error increasing factor.

it=7, (2006-Oct-07)

In this case, we consider the capture in an epoch in which the asteroid has already entered the Earth-Moon system. Fig. 5 contains colour maps of the FC of different tori, covering distances to L_3 from 0.53075 to 0.60047 (a length of about 26800.76 km). Again, the first six maps are coloured according to the minimum distance, in km, reached between the trajectory in the stable manifold and the position of the asteroid, this time at epoch it=7. And the last six maps in Fig. 5 correspond to the same fundamental cylinders but coloured according to the instantaneous Δv in km/s.

In the first fundamental cylinder of Fig. 5 only one minimum distance area is identified, lets call it Minimum 1. However, as we consider fundamental domains of curves increasingly distant to L_3, this minimum is split into two different minimum distance areas. Let us call Minimum 2 to the minimum distance area at higher value of τ. In the third colour map, the first two minima are moving apart and a third one appears for low values of τ, Minimum 3. If we keep on examining fundamental domains of invariant curves further away from L_3, we observe that the third minimum splits into two, naming Minimum 4 the one at lower value of τ. In the fifth colour map, the four minimum distance areas are clearly identified, and for the last colour map Minimum 2 passes to be at the lower part of the fundamental domain. Keep in mind that this is a normal phenomenon since there is a continuity between the boundaries of these maps. The fact that this minimum passes from the upper part of the fundamental domain to the lower part makes necessary to integrate an extra period, see Table 6, since now this initial condition is closer to the invariant curve and it requires more time to approximate the asteroid. Minimum 1 and Minimum 3 come closer as moving through the family of invariant curves of L_3, until they join and then disappear. Concerning to Minimum 2 and Minimum 4, they have been tracked through more invariant curves,

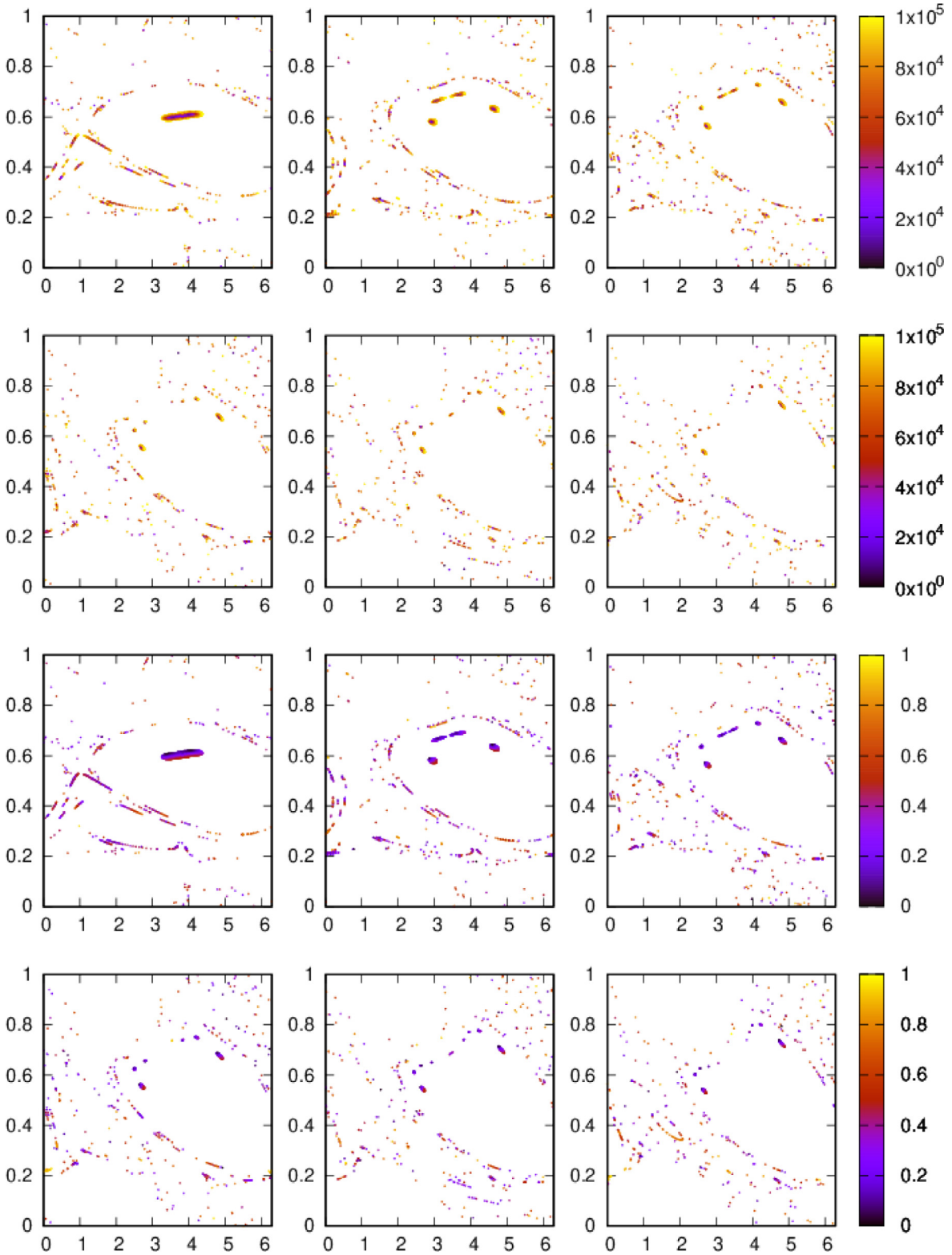

Fig. 3. Six fundamental cylinders of tori at different distances from L_3 between 0.01257 and 0.05784. Plots in the first two rows show the FCs coloured according to the distance to the asteroid at position it=2, in km. Plots in the last two rows show the same FCs this time coloured according to the instantaneous Δv in km/s.

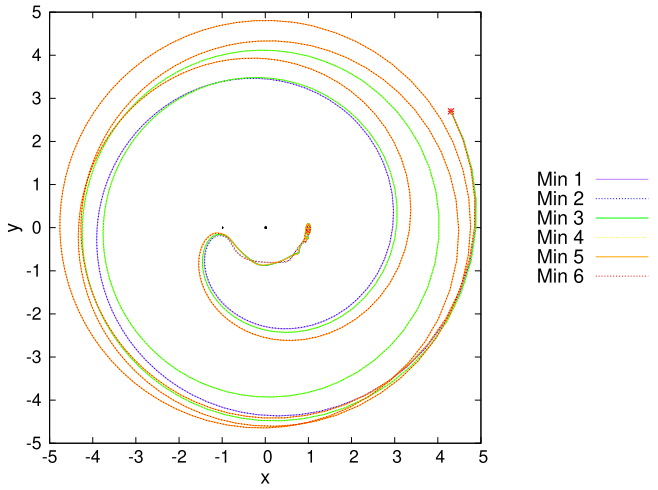

Fig. 4. Simulation of the capture of the asteroid at May 12, 2006, through the trajectories in the stable manifold of the fifth FC of Fig. 3 when applying the obtained Δv, Table 5. The Earth and the Moon are included as black circles of corresponding radius, and the initial position of the asteroid as a red star. (For interpretation of the references to color in this figure legend, the reader is referred to the web version of this article.)

Table 5
Values of θ and τ corresponding to the initial conditions in the fundamental cylinders in Fig. 3, that lay on the position of the asteroid at May 12, 2006, (it=2) after N_T BCP periods, and the Δv required for each of them.

	Min 1				Min 2			
dist to L_3	N_T	θ	τ	Δv (m/s)	N_T	θ	τ	Δv (m/s)
0.01257	5	3.589	0.600	254.159	5	4.029	0.609	254.188
0.02043	5	2.953	0.580	254.098	5	4.654	0.632	254.260
0.03213	5	2.755	0.564	254.045	5	4.826	0.659	254.341
0.03947	5	2.709	0.555	254.018	5	4.849	0.676	254.392
0.04926	5	2.681	0.545	253.986	5	4.839	0.701	254.464
0.05784	5	2.672	0.537	253.962	5	4.805	0.725	254.529
	Min 3				Min 4			
dist to L_3	N_T	θ	τ	Δv (m/s)	N_T	θ	τ	Δv (m/s)
0.01257								
0.02043	6	3.065	0.664	114.391	6	3.702	0.690	114.414
0.03213	6	2.591	0.636	114.346	6	4.149	0.729	114.426
0.03947	6	2.501	0.624	114.320	6	4.216	0.749	114.425
0.04926	6	2.442	0.611	114.283	6	4.237	0.776	114.416
0.05784	6	2.419	0.601	114.248	6	4.222	0.801	114.403
	Min 5				Min 6			
dist to L_3	N_T	θ	τ	Δv (m/s)	N_T	θ	τ	Δv (m/s)
0.01257								
0.02043								
0.03213	7	3.132	0.681	131.324	7	3.506	0.707	131.301
0.03947	7	2.791	0.656	131.348	7	3.827	0.740	131.272
0.04926	7	2.628	0.638	131.366	7	3.958	0.771	131.247
0.05784	7	2.556	0.626	131.379	7	3.997	0.797	131.228

further to L_3 that the six fundamental domain included here, however the Δv needed for using them in a capture increases, see the last map in Fig. 5. Therefore, we only focus on the results of the fundamental cylinders included in the Fig. 5.

As in the previous case, we use a Newton method to find the initial condition (θ and τ on the FC) that arrives to the asteroid 2006 RH120 at epoch it=7. The results are collected in Table 6. It can be observed that the Δv required for the trajectories corresponding to the minimum distance areas 1 and 3 decreases as the curve they belong to is further away from L_3. The opposite effect happens with the trajectories of the minima 2 and 4.

Finally, we take the coordinates of the asteroid at epoch it=7, we add the velocity impulse of Table 6 and we integrate these trajectories forward in time in the planar BCP to check that the asteroid is lead towards L_3 (this is also a final test of correctness of all the computations). In Fig. 6 the trajectories corresponding to the four minimum distance areas of the fifth fundamental cylinder in Fig. 5 are shown. They correspond to an invariant curve for which Minimum 1 and 3 have not yet come together, but it can be appreciated how their trajectories are approaching. For trajectories of Minima 1 and 3 the expansion factor for the error is only of the order 10^2, because they do not approach much any massive body and because

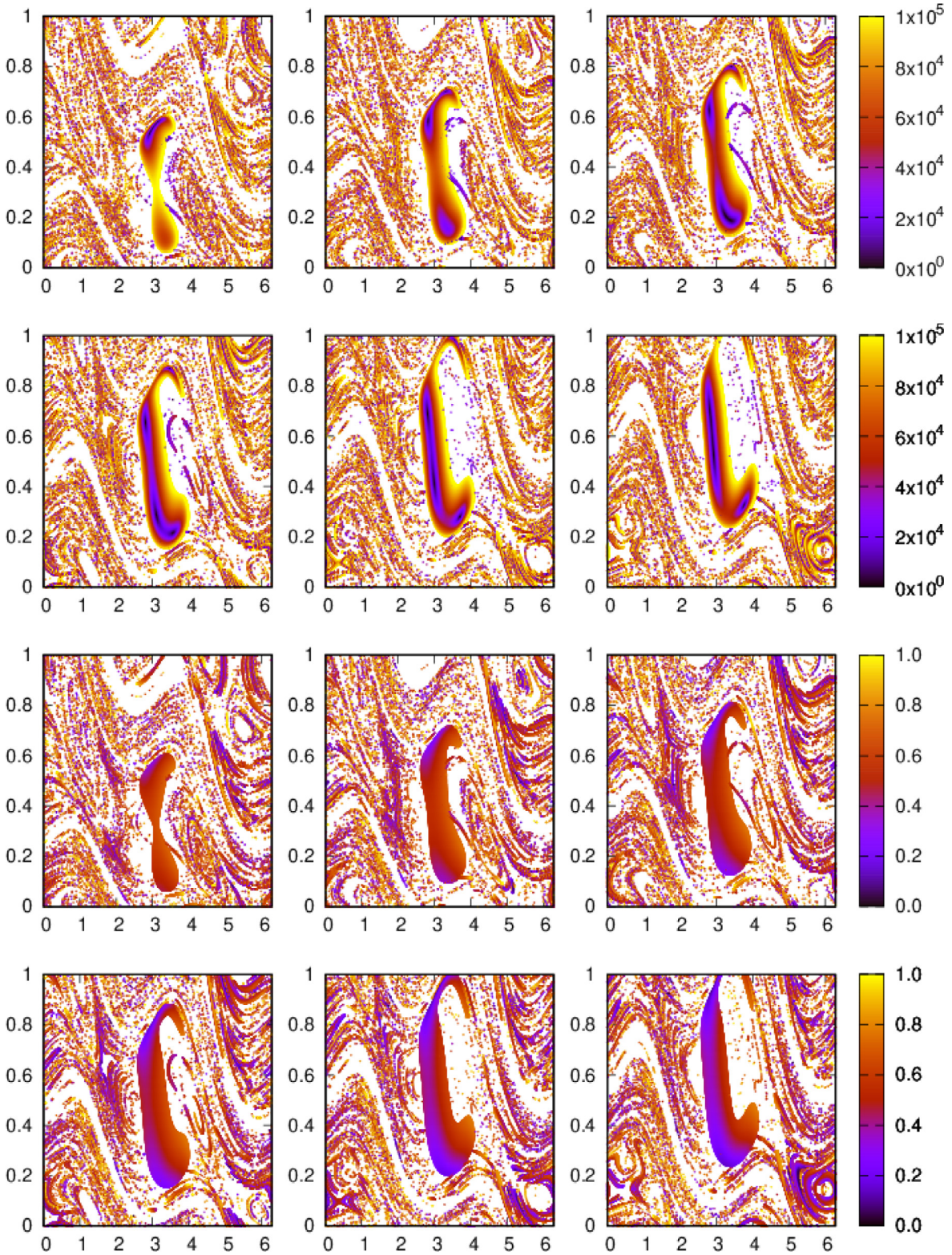

Fig. 5. Six fundamental cylinders of tori at different distances from L_3 between 0.53075 and 0.60047. Plots in the first two rows show the FCs coloured according to the distance to the asteroid at position it=7, in km. Plots in the last two rows show the same FCs this time coloured according to the instantaneous Δv in km/s.

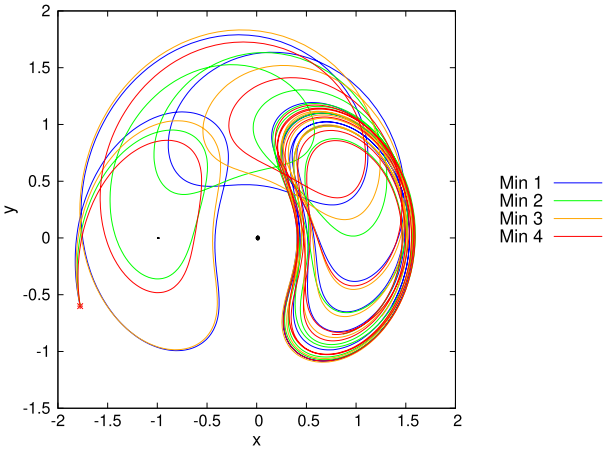

Fig. 6. Simulation of the capture of the asteroid at October 7, 2006, through the trajectories in the stable manifold of the fifth FC of Fig. 5 when applying the obtained Δv, Table 6. The Earth and the Moon are included as black circles of corresponding radius, and the initial position of the asteroid as a red star. (For interpretation of the references to color in this figure legend, the reader is referred to the web version of this article.)

Table 6
Values of θ and τ corresponding to the initial conditions in the fundamental cylinders in Fig. 5, that lay on the position of the asteroid at the October 7, 2006, (it=7) after N_T BCP periods and the Δv required for each of them.

	Min 1				Min 2			
dist to L_3	N_T	θ	τ	Δv (m/s)	N_T	θ	τ	Δv (m/s)
0.53075	6	2.970	0.539	402.596				
0.55281	6	2.867	0.585	388.037	6	3.358	0.702	427.682
0.56617	6	2.844	0.628	379.142	6	3.451	0.800	433.318
0.57624	6	2.840	0.656	373.419	6	3.506	0.870	436.837
0.59139	6	2.850	0.691	365.138	6	3.584	0.985	442.115
0.60047	6	2.872	0.691	360.775	7	4.158	0.021	445.375
	Min 3				Min 4			
dist to L_3	N_T	θ	τ	Δv (m/s)	N_T	θ	τ	Δv (m/s)
0.53075								
0.55281								
0.56617	6	3.307	0.204	406.799				
0.57624	6	3.146	0.285	389.217	6	3.600	0.216	434.045
0.59139	6	3.027	0.420	373.829	6	3.737	0.280	446.723
0.60047	6	2.964	0.533	365.323	6	3.802	0.326	452.982

of the short integration time. This factor is of the order of 10^3 for the trajectory of Minimum 4, and increases to 10^4 for Minimum 2, due to the fact that the trajectory approaches the Moon.

it=14, (2007-May-01)

In this last example of temporal section corresponding to time $t = 0 \bmod T$ (or $t = N_T T$), we show the results for the capture of 2006 RH120 when it is starting to leave the Earth-Moon system. As the evolution of the minimum distance areas between different tori has been detailed in previous cases, from now on the results are presented in a short version. Fig. 7 shows the fundamental cylinders for tori at distances to L_3 from 0.52061 to 0.59139 (a length of $\sim$ 27207.85 km). In the first three FCs, each initial condition is coloured according to the minimum distance, in km, to the position of the asteroid at epoch it=14, and in the last three, they are coloured according to the difference in velocities between the trajectories in the stable manifolds and those of the asteroid, in km/s.

In the first colour map of Fig. 7 a curved minimum distance area seems to appear for high values of τ (if we zoom that region we realise that there are actually two very close minima). As we examine the colour maps corresponding to invariant curves increasingly further away from L_3, the distance between these two separated minima increases: note that they move toward higher values of τ until they appear in the lower part of the fundamental cylinders. When this happens, the trajectories corresponding to those that lay on the exact position of the asteroid, obtained as in the previous cases and collected in Fig. 8 (left), require an extra period of integration. At the right in the same Figure, the trajectories described by the asteroid, starting at epoch it=14 and propagated forward in time after adding the computed Δv for the two minima of the third fundamental cylinder are presented. In this case, the two trajectories approach a little the position of the Moon, specially the red one, for this reason the expansion factor for the error is between $10^3 - 10^4$. Nevertheless, an expansion factor of this value is acceptable.

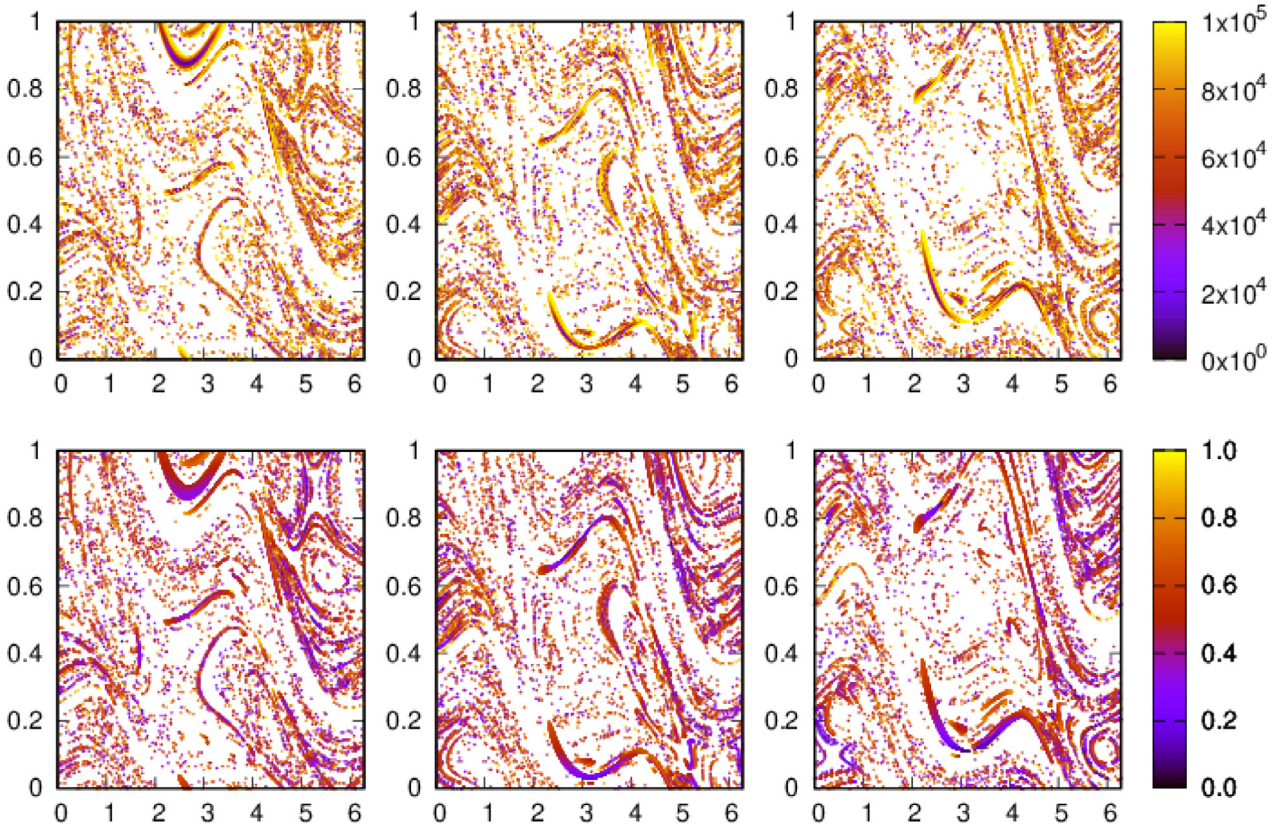

Fig. 7. Three fundamental cylinders of tori at different distances from L_3 between 0.52061 and 0.59139. Plots in the first row show the FCs coloured according to the distance to the asteroid at position it=14, in km. Plots in the last row show the same FCs this time coloured according to the instantaneous Δv in km/s.

	Min 1			
dist to L_3	N_T	θ	τ	Δv (m/s)
0.52061	5	2.551	0.878	362.771
0.56111	6	2.674	0.072	359.814
0.59139	6	2.516	0.197	361.850
	Min 2			
dist to L_3	N_T	θ	τ	Δv (m/s)
0.52061	5	2.845	0.885	370.471
0.52061	6	3.822	0.080	391.813
0.52061	6	4.039	0.205	407.460

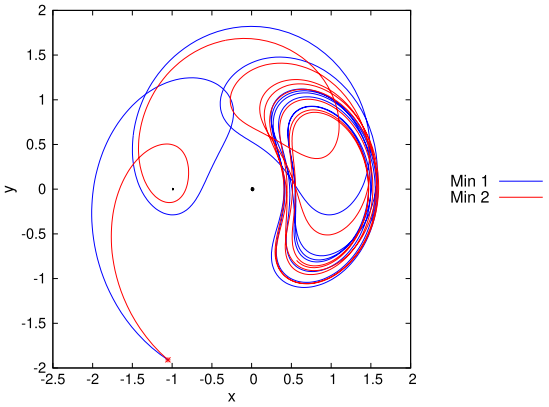

Fig. 8. Left, values of the initial conditions in the FCs of Fig. 7, that after N_T BCP periods lay on the position of the asteroid at May 1, 2007, (it=14), and the Δv required for each of them. Right, simulation of the capture of the asteroid by the trajectories in the minimum distance areas of the third FC when applying the obtained Δv. The Earth is included as a black circle of corresponding radius, and the initial position of the asteroid as a red star. (For interpretation of the references to color in this figure legend, the reader is referred to the web version of this article.)

5.1.1. Temporal continuity

We have performed some computations in order to analyse how the minimum distance area evolve at different time sections, close in time to the temporal section treated in the previous examples. The asteroid was considered twelve hours before and another twelve hours after the three epochs such that the time spans cover one day and are centered in each of the three cases.

For the first case, twelve hours before it=2, the Δv of minima 1, 2, 3 and 4 increases about 10 m/s, however for the minima 5 and 6 it decreases to $\approx$ 120 m/s. When we study these minima twelve hours later than it=2, we see that the

difference in velocities has increased for the six trajectories; about 30 m/s for Minimum 1 and 2, $\approx$ 70 m/s for Minimum 3 and 4 and more than 100 m/s for Minimum 5 and 6.

In the second case, twelve hours before it=7, the Δv grows of the order of a couple of tens of m/s for the four minima. And, twelve hours after it=7, the minimum distance areas do not appear well defined for the first five invariant curves, but the first two minima appear in the fundamental domain corresponding to the last one, requiring less Δv for both; about 20 m/s less for Minimum 1 and about 40 m/s less for Minimum 2.

Finally, for the last case the differences are more homogeneous. Roughly speaking, twelve hours before it=14 the Δv needed is about 20 m/s lower than the one obtained for the two minima studied, and twelve hour after it=14, it increases more or less the same quantity.

Therefore, the same minimum distance areas that are found at a specific temporal section, appear at different close temporal sections, varying a little the difference between the velocities of the trajectories in the stable manifolds and those of the asteroid. This can be used to look for the optimal time (less Δv required) to perform the capture, or to use all these minima, continuous in time, to perform a low thrust. This is left for future work.

5.2. Temporal Poincaré sections at times $T/4$, $T/2$ and $3T/4$

Looking at the variety of possible trajectories for the capture of asteroid 2006 RH120 offered by the stable manifolds of the invariant curves of L_3, it is expected that many other possibilities appear when applying the same strategy for the capture at temporal Poincaré sections corresponding to $T/4$, $T/2$ and $3T/4$.

Actually, several new minimum distance areas have been found for any of these three temporal sections and for the different epochs of the asteroid. We do not aim to present neither all the possibilities nor different cases for any of the temporal sections, but to give some representative results in a qualitative way and to explain, quantitatively, a couple of examples.

First, we discuss the situation where the asteroid has not still entered the Earth-Moon system. Regardless of the temporal section applied, the obtained colour maps corresponding to fundamental cylinders of the inner tori in the family, are very similar to those presented in Fig. 3, with some variations in the required Δv. This is in good agreement with the temporal continuity of the minimum distance areas exposed in Section 5.1.1.

Notice that the fact that these minimum distance areas are present in the fundamental cylinders of inner tori covering a time span of more than three months and different temporal section, implies a long continuity in time of these possibilities of capture, which is good. The reason for this to happen is that the trajectories in the stable invariant manifolds that are far from the Earth and the Moon, are orbiting the Earth-Moon system while approaching it, the same behaviour is shown by the asteroid before entering the system. Therefore, the trajectory of the asteroid and the trajectories on the stable manifolds of L_3 are continually meeting before finally entering the system, where they may behave differently.

In fact, such a long temporal continuity is not found for any of the other minimum distance areas corresponding to epochs in which the asteroid is inside the system. What we have observed for these epochs is a decrease in the required Δv, being in many cases even lower than 200 m/s. However, for these new temporal sections, less possibilities are available for the epochs in with the asteroid is leaving the system.

Finally, we present two cases, the first one concerns to the lowest Δv found for the epochs in which the asteroid has not entered yet the system, and the second one is devoted to an example of relative low Δv when the asteroid is already inside the system.

A very cheap transfer

If we look closely to the maps in Fig. 3, we can observe that in the minimum distance areas, the trajectory corresponding to the one that lays on the position of the asteroid is placed, roughly speaking, in the centre of zone, however, when we look at the same colour maps coloured according to the Δv, we see that the minimum value of Δv for those areas is not placed at their centres. It happens that half a period after epoch it=3, the minimum in distance and the minimum in Δv more or less overlap for the first two minima of the six observed, leading to trajectories that require less than 20 m/s for the capture.

In Fig. 9 we show some fundamental cylinders of tori close to L_3, at distances from 0.02159 to 0.03947. The first three maps are coloured according to the distance between the position of the asteroid at the 25 of June of 2006 (half a period after epoch it=3) and the trajectories in the stable manifolds at the temporal section $T/2$; the other three colour maps are coloured according to the difference between velocities. It is easy to observe that the required Δv has decreased significantly for the first bigger minima, but not for the other four. Fig. 10 (left) contains the table with the data for the initial conditions in the FCs, corresponding to those two minima, that leads to the trajectories laying on the position of the asteroid, together with the trajectories described by the asteroid, forward in time, after adding the velocity impulse of the third presented fundamental cylinder. These trajectories not only require a very low Δv but also do not come close to any of the primaries, suggesting a safe and very cheap journey for the asteroid.

A last example

Fig. 11 shows some fundamental cylinders for tori at distances from L_3 between 0.44160 and 0.53075. In the first three plots, the initial conditions are coloured according to the distance between the position of the asteroid at the 14 of October

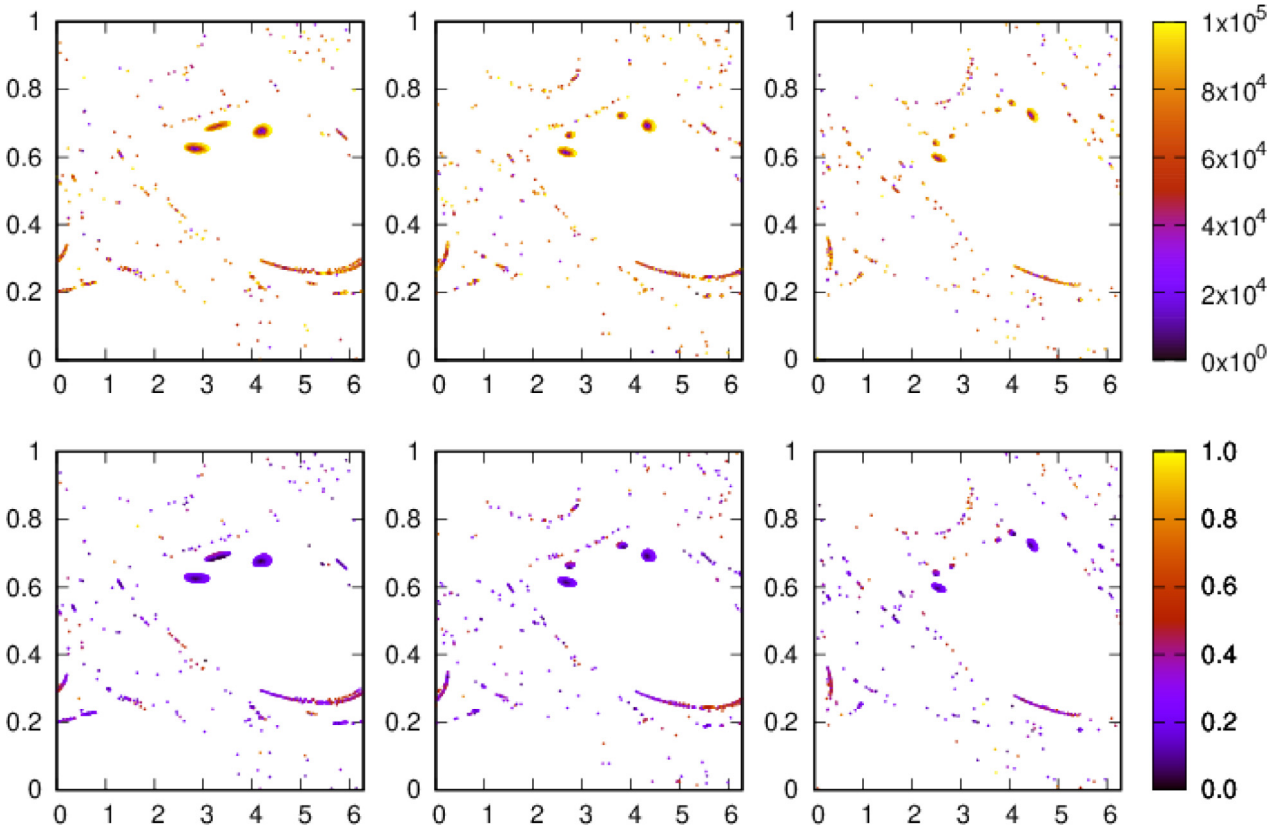

Fig. 9. Three fundamental cylinders of tori at different distances from L_3 between 0.02159 and 0.03947. Plots in the first row show the FCs coloured according to the distance to the asteroid $T/2$ after position it=3, in km. Plots in the last row show the same FCs this time coloured according to the instantaneous Δv in km/s.

	Min 1			
dist to L_3	N_T	θ	τ	Δv (m/s)
0.02159	4	2.856	0.626	19.398
0.02738	4	2.693	0.615	19.386
0.03947	4	2.555	0.597	19.338
	Min 2			
dist to L_3	N_T	θ	τ	Δv (m/s)
0.02159	4	4.224	0.678	19.338
0.02738	4	4.373	0.693	19.293
0.03947	4	4.472	0.725	19.176

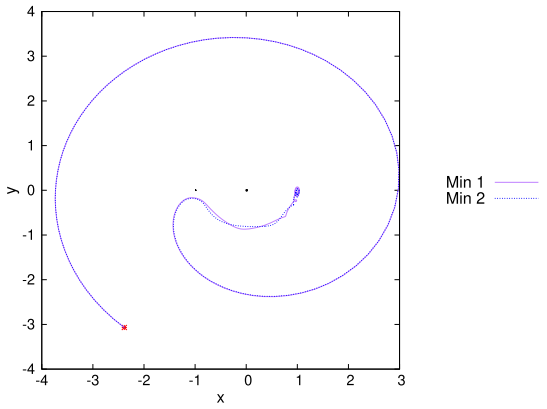

Fig. 10. Left, values of the initial conditions in the FCs of Fig. 9, that after N_T BCP periods lay on the position of the asteroid at June 25, 2006, (half a period after it=3) and the Δv required for each of them. Right, simulation of the capture of the asteroid by the trajectories in the two bigger minimum distance areas on the third FC when applying the obtained Δv. The Earth and the Moon are included as black circles of corresponding radius, and the initial position of the asteroid as a red star. (For interpretation of the references to color in this figure legend, the reader is referred to the web version of this article.)

of 2006 (a quarter of period after epoch it=7) and the trajectories in the stable manifolds at temporal section $T/4$; the other three maps correspond to the same FCs, now coloured according to the difference between their velocities. Two minima are found, for one of them, the Δv increases with the distance to L_3, and for the other one, it decreases. As before, we have refined trajectories near these minima that arrive exactly to the asteroid, the results are collected in Fig. 12, left. At the right of this figure, the trajectories corresponding to the integration of the asteroid forward in time, after adding a velocity

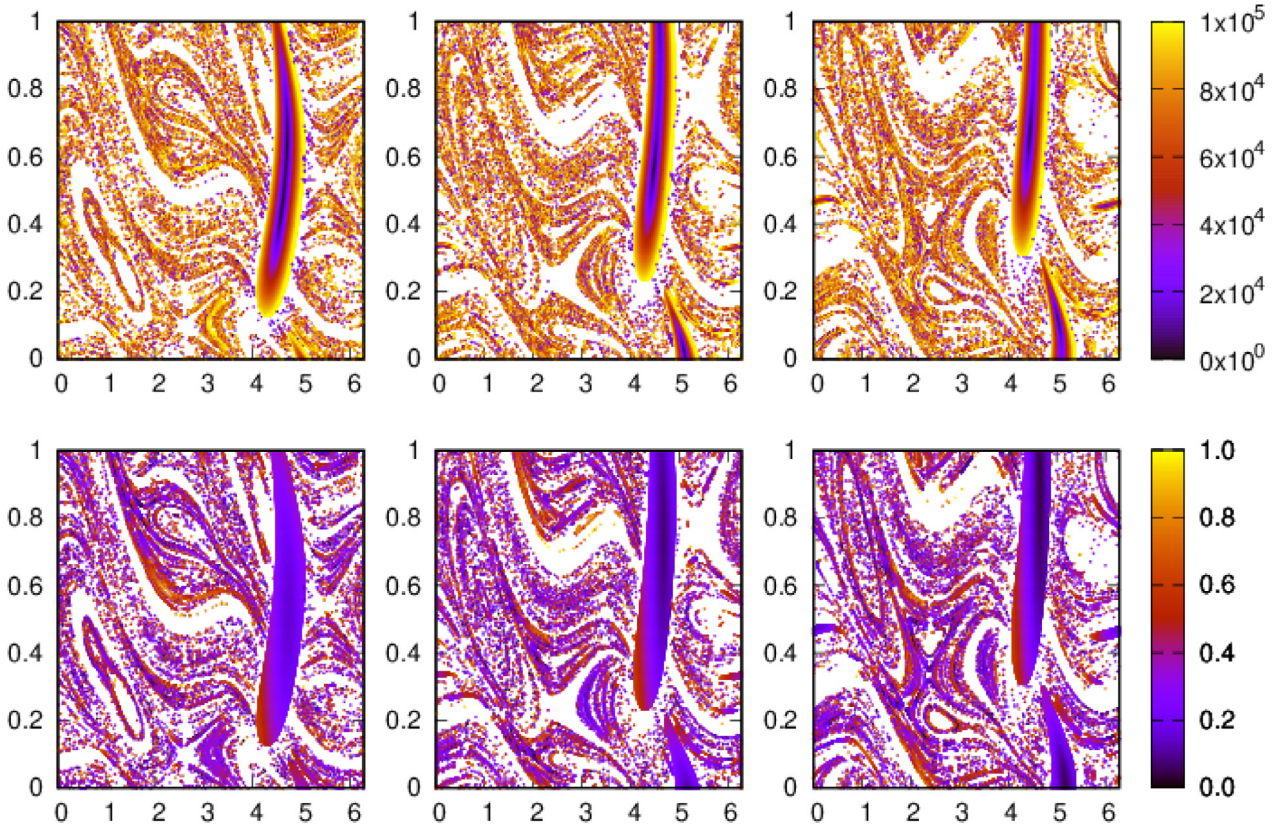

Fig. 11. Three fundamental cylinders of tori at different distances from L_3 between 0.44160 and 0.53075. Plots in the first row show the FCs coloured according to the distance to the asteroid $T/4$ after position it=7, in km. Plots in the last row show the same FCs this time coloured according to the instantaneous Δv in km/s.

	Min 1			
dist to L_3	N_T	θ	τ	Δv (m/s)
0.44160	4	4.645	0.453	186.195
0.50037	4	4.517	0.560	204.122
0.53075	4	4.481	0.666	213.989
	Min 2			
dist to L_3	N_T	θ	τ	Δv (m/s)
0.44160	4	4.743	0.635	170.133
0.50037	5	5.137	0.026	148.754
0.53075	5	5.067	0.116	144.139

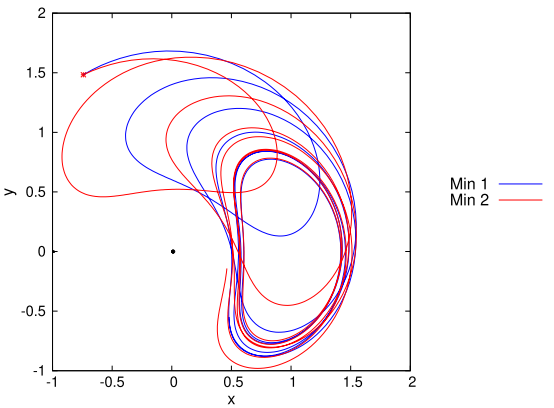

Fig. 12. Left, values of the initial conditions in the FCs of Fig. 11, that after N_T BCP periods lay on the position of the asteroid at October 14, 2006, (a quarter of period after it=7), and the Δv required for each of them. Right, simulation of the capture of the asteroid by the trajectories in the minimum distance areas on the third FC when applying the obtained Δv. The Earth is included as a black circle of corresponding radius, and the initial position of the asteroid as a red star. (For interpretation of the references to color in this figure legend, the reader is referred to the web version of this article.)

impulse to reach the third fundamental domain are also included. In this last example, the asteroid is so close to the family of tori around L_3 that the trajectories are pretty short.

6. Conclusions

This paper presents a strategy for capturing a NEA in a neighbourhood of the L_3 point of the Earth-Moon system. It is based on the use of stable invariant manifolds of invariant tori around L_3 of the planar Bicircular Earth-Moon system. To

compute the manifolds we first obtain a high order approximation to them by combining jet transport and the parametrization method, and then we globalise them by means of numerical integration. This shows that a part of these manifolds exits the Earth-Moon system and then orbits the Sun in a trajectory close to that of the Earth around the Sun, which intersects the region of motion of NEAs. When these manifolds intersect with the position of a NEA, the difference between their velocities (Δv) gives the necessary manoeuvre to inject the NEA in the manifold so that it travels to the neighbourhood of L_3. For a NEA following an orbit similar to that of the Earth, this difference of velocities should not be very large.

We have applied this procedure to study the capture of the asteroid 2006 RH120. In general, several possibilities for the capture have been found, for the different positions of the asteroid and for the different temporal Poincaré maps applied to the stable manifolds. As expected, the Δv varies depending on the relative position of the asteroid with respect to the massive bodies in the system, being higher when the asteroid is inside the Earth-Moon system and significantly lower when it is still outside. In fact, one option for the capture that only requires a manoeuvre of less than 20 m/s has been analysed.

In addition, it has been observed that the possibilities for the capture vary continuously between nearby tori in the family and also depend continuously in time. This suggest that the dynamics below these opportunities is robust. Moreover, these continuities can be exploited to perform optimisation methods and reduce, even more, the required Δv.

We want to emphasise that this machinery is valid for studying the capture of any other asteroid or space debris with an orbit close to that of the Earth. It is also possible to use other families of quasi-periodic orbits as a target destination for the captured object, and it may also be a tool to analyse the deflection of NEAs (with an orbit close to that of the Earth) that pose a collision threat to the Earth.

Finally, let us comment on some extensions of this work. The next natural steps are to use the 3D Bicircular model, to refine the transfer trajectory and the destination orbit near L_3 to a realistic model (for instance, based on the JPL ephemeris), and to consider the use of a low thrust propulsion system for the transfer manoeuvre. These are work in progress.

Credit author statement

A. Jorba and B. Nicolás are the sole authors of this work, and are equally responsible for the contents of this manuscript. For this reason the authors appear in alphabetical order.

Declaration of Competing Interest

The authors declare that they have no known competing financial interests or personal relationships that could have appeared to influence the work reported in this paper.

Acknowledgment

This work has been supported by the Spanish grants PGC2018-100699-B-I00 (MCIU/AEI/FEDER, UE) and the Catalan grant 2017 SGR 1374. The project leading to this application has received funding from the European Union's Horizon 2020 research and innovation programme under the Marie Skłodowska-Curie grant agreement No 734557. B. Nicolás is supported by the Ministry of Economy, Industry and Competitiveness of Spain through the National Plan for I+D+i (MTM2015-67724-R) and through the national scholarship BES-2016-078722.

References

[1] Andrews DG, Bonner KD, Butterworth AW, Calvert HR, Dagang BRH, Dimond KJ, Eckenroth LG, Erickson JM, Gilbertson BA, Gompertz NR, Igbinosun OJ, Ip TJ, Khan BH, Marquez SL, Neilson NM, Parker CO, Ransom EH, Reeve BW, Robinson TL, Rogers M, Schuh PM, Tom CJ, Wall SE, Watanabe N, Yoo CJ. Defining a successful commercial asteroid mining program. Acta Astron 2015;108:106–18. doi:10.1016/j.actaastro.2014.10.034. https://www.sciencedirect.com/science/article/pii/S0094576514004123

[2] Armellin R, Di Lizia P, Bernelli-Zazzera F, Berz M. Asteroid close encounters characterization using differential algebra: the case of Apophis. Celest Mech Dyn Astron 2010;107(4):451–70. doi:10.1007/s10569-010-9283-5.

[3] Alessi EM, Farrés A, Jorba A, Simó C, Vieiro A. Efficient usage of self validated integrators for space applications. Ariadna Final Report, Contract No. 20783/07/NL/CB. ESTEC (European Space Agency); 2008.

[4] Alessi EM, Farrés A, Jorba A, Simó C, Vieiro A. Jet transport and applications to NEOs. In: Proceedings of the 1st IAA planetary defense conference: protecting earth from asteroids, Granada (Spain); 2009.

[5] Andreu MA. Dynamics in the center manifold around L_2 in the quasi-bicircular problem. Celest Mech Dyn Astron 2002;84(2):105–33.

[6] Berz M, Makino K. Verified integration of ODEs and flows using differential algebraic methods on high-order Taylor models. Reliab Comput 1998;4:361–9. doi:10.1023/A:1024467732637.

[7] Cabré X, Fontich E, de la Llave R. The parameterization method for invariant manifolds. III. Overview and applications. J Differ Equ 2005;218(2):444–515. doi:10.1016/j.jde.2004.12.003.

[8] Castellà E, Jorba A. On the vertical families of two-dimensional tori near the triangular points of the Bicircular problem. Celest Mech Dyn Astron 2000;76(1):35–54.

[9] Cronin J, Richards PB, Russell LH. Some periodic solutions of a four-body problem. Icarus 1964;3:423–8.

[10] Franceschini V, Russo L. Stable and unstable manifolds of the Hénon mapping. J Statist Phys 1981;25(4):757–69.

[11] Folta D, Vaughn F. A survey of earth-moon libration orbits: stationkeeping strategies and intra-orbit transfers. In: Proceedings of the AIAA/AAS astrodynamics specialist conference and exhibit, Providence, Rhode Island; 2004.

[12] Gabern F, Jorba A. Generalizing the restricted three-body problem. The Bianular and Tricircular coherent problems. Astron Astrophys 2004;420:751–62.

[13] Gimeno J., Jorba A., Jorba-Cuscó M., Miguel N., Zou M.. Numerical integration of high order variational equations of ODEs; 2021. Preprint.

[14] Gómez G, Llibre J, Martínez R, Simó C. Dynamics and mission design near libration points. Vol. I, Fundamentals: the case of collinear libration points. World Scientific Monograph Series in Mathematics, vol. 2. World Scientific Publishing Co. Inc.; 2001. ISBN 981-02-4285-9.

[15] Griewank A. Evaluating derivatives. Philadelphia, Penn: SIAM; 2000. ISBN 0-89871-451-6.
[16] Haro A, Canadell M, Luque A, Mondelo J-M, Figueras JL. The parameterization method for invariant manifolds. From rigorous results to effective computations. Applied Mathematical Sciences, vol. 195. Springer-Verlag; 2016.
[17] Haro A, de la Llave R. A parameterization method for the computation of invariant tori and their whiskers in quasi-periodic maps: rigorous results. J Differ Equ 2006;228(2):530–79. doi:10.1016/j.jde.2005.10.005.
[18] Huang SS. Very restricted four-body problem. Technical note TN D-501. Goddard Space Flight Center, NASA; 1960. https://ntrs.nasa.gov/archive/nasa/casi.ntrs.nasa.gov/19890068606.pdf
[19] Jorba-Cuscó M, Farrés A, Jorba A. Two periodic models for the Earth-Moon system. Front Appl Math Stat 2018;4:32. doi:10.3389/fams.2018.00032.
[20] Jorba-Cuscó M, Farrés A, Jorba A. On the stabilizing effect of Solar radiation pressure in the Earth-Moon system. Adv Space Res 2021;67(9):2812–22. doi:10.1016/j.asr.2020.01.017. https://www.sciencedirect.com/science/article/pii/S0273117720300351
[21] Jorba A, Nicolás B. Transport and invariant manifolds near L_3 in the Earth-Moon Bicircular model. Commun Nonlinear Sci Numer Simul 2020;89:105327. doi:10.1016/j.cnsns.2020.105327.
[22] Jorba A. A numerical study on the existence of stable motions near the triangular points of the real Earth-Moon system. Astron Astrophys 2000;364(1):327–38.
[23] Jorba A. Numerical computation of the normal behaviour of invariant curves of n-dimensional maps. Nonlinearity 2001;14(5):943–76.
[24] JPL-Hor. https://ssd.jpl.nasa.gov/?horizons.
[25] Jorba A, Villanueva J. On the normal behaviour of partially elliptic lower dimensional tori of Hamiltonian systems. Nonlinearity 1997;10:783–822.
[26] Jorba A, Villanueva J. On the persistence of lower dimensional invariant tori under quasi-periodic perturbations. J Nonlinear Sci 1997;7:427–73.
[27] Jorba A, Zou M. A software package for the numerical integration of ODEs by means of high-order Taylor methods. Exp Math 2005;14(1):99–117.
[28] Kwiatkowski T, Kryszczyńska A, Polińska M, Buckley DAH, O'Donoghue D, Charles PA, Crause L, Crawford S, Hashimoto Y, Kniazev A, Loaring N, Romero Colmenero E, Sefako R, Still M, Vaisanen P. Photometry of 2006 RH120: An asteroid temporary captured into a geocentric orbit. Astron Astrophys 2009;495(3):967–74. doi:10.1051/0004-6361:200810965.
[29] Mazanek DD, Merrill RG, Brophy JR, Mueller RP. Asteroid redirect mission concept: a bold approach for utilizing space resources. Acta Astron 2015;117:163–71. doi:10.1016/j.actaastro.2015.06.018. https://www.sciencedirect.com/science/article/pii/S0094576515002635
[30] O'Leary B. Mining the Apollo and Amor asteroids. Science 1977;197(4301):363–6. doi:10.1126/science.197.4301.363-a. https://science.sciencemag.org/content/197/4301/363.2
[31] Rosales JJ, Jorba A, Jorba-Cuscó M. Families of Halo-like invariant tori around L_2 in the Earth-Moon Bicircular problem. Celest Mech Dyn Astron 2021;133(4):16. doi:10.1007/s10569-021-10012-0.
[32] Simó C, Gómez G, Jorba A, Masdemont J. The Bicircular model near the triangular libration points of the RTBP. In: Roy AE, Steves BA, editors. From Newton to Chaos. New York: Plenum Press; 1995. p. 343–70.
[33] Sánchez JP, García Yárnoz D, Alessi EM, McInnes CR. Gravitational capture opportunities for asteroid retrieval missions. In: Proceedings of the 63nd international astronautical congress, Naples (Italy); 2012.
[34] Sánchez JP, Neves R, Urrutxua H. Trajectory design for asteroid retrieval missions: a short review. Front Appl Math Stat 2018;4:44. doi:10.3389/fams.2018.00044.
[35] Tan M, McInnes C, Ceriotti M. Direct and indirect capture of near-Earth asteroids in the Earth-Moon system. Celest Mech Dyn Astron 2017;129:57–88. doi:10.1007/s10569-017-9764-x.
[36] Urrutxua H, Scheeres D, Bombardelli C, Gonzalo JL, Pelaez J. What does it take to capture an asteroid? A case study on capturing asteroid 2006 RH120. Adv Astronaut Sci 2014;152:1117–36.
[37] Vergaaij M, McInnes CR, Ceriotti M. Economic assessment of high-thrust and solar-sail propulsion for near-earth asteroid mining. Adv Space Res 2020;67(9):3045–58. doi:10.1016/j.asr.2020.06.012. https://www.sciencedirect.com/science/article/pii/S0273117720304142
[38] Wilczak D, Zgliczyński P. Cr-Lohner algorithm. Schedae Informaticae 2012;2011(20):9–42. https://www.ejournals.eu/Schedae-Informaticae/2011/Volume-20/art/1201/